

1 **Sensitivity of cloud phase distribution to cloud microphysics and**
2 **thermodynamics in simulated deep convective clouds and SEVIRI**
3 **retrievals**

4 Cunbo Han^{1,2}, Corinna Hoose¹, Martin Stengel³, Quentin Coopman⁴, Andrew Barrett¹

5

6 1. Institute of Meteorology and Climate Research (IMK-TRO), Karlsruhe Institute of
7 Technology, Karlsruhe, Germany

8 2. State Key Laboratory of Tibetan Plateau Earth System, Environment and
9 Resources (TPESER), Institute of Tibetan Plateau Research, Chinese Academy
10 of Sciences, Beijing, China

11 3. Deutscher Wetterdienst (DWD), Offenbach, Germany

12 4. Department of Atmospheric and Oceanic Sciences, McGill University, Montreal,
13 Canada

14

15

16

17

18

19 Correspondence to: Cunbo Han (cunbo.han@hotmail.com) and Corinna Hoose
20 (corinna.hoose@kit.edu)

21

22

删除了: Now at

24 **Abstract:**

25 The formation of ice in clouds is an important process in mixed-phase clouds, and
26 the radiative properties and dynamical developments of clouds strongly depend on
27 their partitioning between liquid and ice phases. In this study, we investigate the
28 sensitivities of the cloud phase to ice-nucleating particle (INP) concentration and
29 thermodynamics. Experiments are conducted using the ICOSahedral Nonhydrostatic
30 model (ICON) at the convection-permitting resolution of about 1.2 km on a domain
31 covering significant parts of central Europe, and are compared to two different
32 retrieval products based on SEVIRI measurements. We select a day with **multiple**,
33 isolated deep convective clouds, reaching a homogeneous freezing temperature at
34 the cloud top. The simulated cloud liquid pixel fractions are found to decrease with
35 increasing INP concentration both within clouds and at the cloud top. The decrease
36 in cloud liquid pixel fraction is not monotonic but is stronger in high INP cases.
37 Cloud-top glaciation temperatures shift toward warmer temperatures with increasing
38 INP concentration by as much as 8 °C. Moreover, the impact of INP concentration on
39 cloud phase partitioning is more pronounced at the cloud top than within the cloud.
40 Moreover, initial and lateral boundary temperature fields are perturbed with
41 increasing and decreasing temperature increments from 0 to +/-3K and +/-5K
42 between 3 and 12 km. Perturbing the initial thermodynamic state is also found to
43 affect the cloud phase distribution systematically. However, the simulated cloud-top
44 liquid pixel fraction, diagnosed using radiative transfer simulations as input to a
45 satellite forward operator and two different satellite remote sensing retrieval
46 algorithms, deviates from one of the satellite products regardless of perturbations in
47 the INP concentration or the initial thermodynamic state for warmer sub-zero
48 temperatures, while agreeing with the other retrieval scheme much better, in
49 particular for the high INP and high convective available potential energy (CAPE)
50 scenarios. Perturbing the initial thermodynamic state, which artificially increases the
51 instability of the mid- and upper-troposphere, brings the simulated cloud-top liquid
52 pixel fraction closer to the satellite observations, especially in the warmer mixed-
53 phase temperature range.

54
55 **Keywords:** Mixed-phase clouds, deep convection, INP, thermodynamics, satellite
56 forward operator, remote-sensing retrieval algorithms

删除了: several

删除了: number

删除了: number

删除了: number

删除了: number

62

63 **Key points:**

- 64 1. Cloud properties are retrieved using a satellite forward operator and remote
65 sensing retrieval algorithms with ICON simulations as input. To our knowledge,
66 it is the first time this approach has been used to retrieve cloud phase and other
67 microphysical variables.
- 68 2. Glaciation temperature shifts towards a warmer temperature with increasing
69 INP concentration both within the cloud and at the cloud top. Initial
70 thermodynamic states affect the cloud phase distribution significantly as well.
- 71 3. Simulated cloud-top liquid pixel fraction matches the satellite observations in
72 the high INP and high CAPE scenarios.

73

删除了: number

75 **1. Introduction**

76 In the temperature range between 0 and -38°C, ice particles and supercooled liquid
77 droplets can coexist in mixed-phase clouds. Mixed-phase clouds are ubiquitous in
78 Earth's atmosphere, occurring at all latitudes from the poles to the tropics. Because
79 of their widespread nature, mixed-phase processes play a critical role in the life cycle
80 of clouds, precipitation formation, cloud electrification, and the radiative energy
81 balance on both regional and global scales ([Korolev et al., 2017](#)). Deep convective
82 clouds are always mixed-phase clouds, and their cloud tops reach the homogeneous
83 freezing temperature, -38°C, in most cases. Despite the importance of mixed-phase
84 clouds in shaping global weather and climate, microphysical processes for mixed-
85 phase cloud formation and development are still poorly understood, especially ice
86 formation processes. It is not surprising that the representation of mixed-phase
87 clouds is one of the big challenges in weather and climate models ([McCoy et al.,
88 2016](#); [Korolev et al., 2017](#); [Hoose et al., 2018](#); [Takeishi and Storelvmo, 2018](#); [Vignon
89 et al., 2021](#); [Zhao et al., 2021](#)).

90
91 The distribution of cloud phase has been found to impact cloud thermodynamics and
92 Earth's radiation budget significantly ([Korolev et al., 2017](#); [Matus and L'Ecuyer,
93 2017](#); [Hawker et al., 2021](#)). The freezing of liquid droplets releases latent heat and
94 hence affects the thermodynamic state of clouds. Moreover, distinct optical
95 properties of liquid droplets and ice particles exert different impacts on cloud's
96 shortwave and longwave radiation. [Simulation and observation studies reported that
97 the cloud phase in the mixed-phase temperature range of convective clouds is
98 influenced by aerosol and plays a significant role in the development into deeper
99 convective systems](#) ([Li et al., 2013](#); [Sheffield et al., 2015](#); [Mecikalski et al., 2016](#)).

100 Observational studies reveal that the cloud phase distribution is highly temperature-
101 dependent and influenced by multiple factors, for example, cloud type and cloud
102 microphysics ([Rosenfeld et al., 2011](#); [Coopman et al., 2020](#)). Analyzing passive
103 satellite observations of mixed-phase clouds over the Southern Ocean, [Coopman et
104 al. \(2021\)](#) found that cloud ice fraction increases with increasing cloud effective
105 radius. Analysis of both passive and active satellite datasets reveals an increase in
106 supercooled liquid fraction with cloud optical thickness ([Bruno et al., 2021](#)).

107

108 A number of in-situ observations of mixed-phase clouds have been made in the past
109 several decades, covering stratiform clouds (Pinto, 1998; Korolev and Isaac, 2006;
110 Noh et al., 2013) and convective clouds (Rosenfeld and Woodley, 2000; Stith et al.,
111 2004; Taylor et al., 2016). Aircraft-based observations of mixed-phase clouds
112 properties reveal that the frequency distribution of the ice water fraction has a U-
113 shape, with two explicit maxima, one for ice water fraction smaller than 0.1 and the
114 other for ice water fraction larger than 0.9, and the frequency of occurrence of mixed-
115 phase clouds is approximately constant when the ice water fraction is in the range
116 between 0.2 and 0.5 (Korolev et al., 2003; Field et al., 2004; Korolev et al., 2017).
117 These findings are very useful constraints of numerical models (Lohmann and
118 Hoose, 2009; Grabowski et al., 2019). However, in-situ observations of mixed-phase
119 cloud microphysics are technically difficult and sparse in terms of spatial and
120 temporal coverage. Thus, understanding ice formation processes and determining
121 the climatological significance of mixed-phase clouds have proved difficult using
122 existing in-situ observations only.

123
124 Both observations and simulations reveal that ice-nucleating particles (INPs) impact
125 deep convective cloud properties including the persistence of deep convective
126 clouds and precipitation (Twohy, 2015; Fan et al., 2016). However, the impact of
127 INPs on precipitation from deep convective clouds is still uncertain and may depend
128 on precipitation and cloud types (van den Heever et al., 2006; Min et al., 2009; Fan
129 et al., 2010; Li and Min, 2010). Although the effects of INPs on convective
130 precipitation are not conclusive, it is certain that the interactions between convective
131 clouds and INPs affect cloud microphysical properties and hence cloud phase
132 distributions. In addition, previous numerical modeling studies on cloud-aerosols
133 interactions have focused on influences of aerosols acting as cloud condensation
134 nuclei (CCN) (Fan et al., 2016), which are linked to the ice phase e.g. through
135 impacts on the riming efficiency (Barrett and Hoose, 2023). Given the limited
136 knowledge on ice formation in deep convective clouds and significant uncertainties in
137 ice nucleation parameterizations, it is necessary to conduct sensitivity simulations to
138 investigate how ice formation processes are influenced by INP concentrations and
139 thermodynamic states in deep convective clouds.

删除了： ,

删除了： with the occurrence of mixed-phase clouds decreasing toward lower temperatures

删除了： Satellite observations indicate that dust serves as effective INPs in the Saharan air layer, promotes the heterogeneous ice nucleation process, shifts the precipitation size distribution from large to small raindrops in deep convective clouds, and ultimately reduces precipitation

删除了： . However, the convection-permitting simulations by (van den Heever et al., 2006) showed (van den Heever et al., 2006) showed that convective precipitation increases with increasing INPs. Moreover, some simulation studies argue that dust aerosols acting as INPs have hardly any effect on convective precipitation although they significantly impact cloud microphysical properties (Fan et al., 2010). (Li and Min, 2010) suggested that the impacts of INPs on deep convective precipitation systems highly depend on the precipitation type.

删除了： (van den Heever et al., 2006) showed that precipitation increases with increasing INPs. Moreover, some simulation studies argue that dust aerosols acting as INPs have hardly any effect on convective precipitation although they significantly impact cloud microphysical properties (Fan et al., 2010). (Li and Min, 2010) suggested that the impacts of INPs on deep convective precipitation systems highly depend on the precipitation type.

设置了格式： 英语(美国)

170 In this study, with the help of realistic convection-permitting simulations using two-
171 moment microphysics, we address how and to what extent INP concentration and
172 thermodynamic state affect the in-cloud and cloud-top phase distributions in deep
173 convective clouds. In particular, cloud properties are retrieved using a satellite
174 forward operator and remote sensing retrieval algorithms with radiative transfer
175 simulations as input for a fair comparison to observations from SEVIRI. This method
176 allows us to compare model simulated cloud properties with remote sensing cloud
177 products directly, and is, to our knowledge, the first time this approach is used for the
178 cloud phase and related microphysical variables. We aim to evaluate the satellite
179 retrieval algorithms and investigate whether passive satellite cloud products can
180 detect cloud microphysical and thermodynamical perturbations.

182 This paper is structured as follows: In section 2, we introduce our model setups and
183 the experiment design, the satellite forward operator, remote sensing retrieval
184 algorithms, and datasets. Simulation results for the sensitivity experiments are
185 shown in section 3. Section 4 presents discussions; and we summarize the study
186 and draw conclusions in section 5.

187 2. Data and Method

188 2.1. Model description

189 The Icosahedral Nonhydrostatic (ICON) model ([Zängl et al., 2015](#)) is a state-of-the-
190 art unified modeling system offering three physics packages, which are dedicated to
191 numerical weather prediction (NWP), climate simulation, and large-eddy simulation.
192 ICON is a fully compressible model and has been developed collaboratively between
193 the German Weather Service (DWD), Max Planck Institute for Meteorology, German
194 Climate Computing Center (DKRZ), and Karlsruhe Institute of Technology (KIT). In
195 order to maximize the model performance and to remove the singularity at the poles,
196 ICON solves the prognostic variables suggested by [Gassmann and Herzog \(2008\)](#),
197 on an unstructured triangular grid with C-type staggering based on a successive
198 refinement of a spherical icosahedron ([Wan et al., 2013](#)). Governing equations are
199 described in [Wan et al. \(2013\)](#) and [Zängl et al. \(2015\)](#). The DWD has operated the
200 ICON model at a spatial resolution of about 13 km on the global scale since January
201 2015. In the global ICON, the higher-resolution ICON-EU (resolution 7 km) nesting

下移了 [1]: A similar strategy was used by [Kay et al. \(2018\)](#) for the evaluation of precipitation in a climate model with CloudSat observations and termed "scale-aware and definition-aware evaluation". [Stengel et al. \(2020\)](#) applied a cloud classification algorithm developed for satellite observations to model simulated brightness temperatures in a similar manner.

211 area for Europe has been embedded since July 2015. In this study, ICON-2.6.4 with
212 the NWP physics package is used and initial and lateral boundary conditions are
213 provided by the ICON-EU analyses.

214

215 For cloud microphysics, we use an updated version of the two-moment cloud
216 microphysics scheme developed by [Seifert and Beheng \(2006\)](#). The two-moment
217 scheme predicts the number and mass mixing ratios of two liquid (cloud and rain)
218 and four solid (ice, graupel, snow, and hail) hydrometers. The cloud condensation
219 nuclei (CCN) activation is described following the parameterization developed by
220 [Hande et al. \(2016\)](#). Homogeneous freezing, including freezing of liquid water
221 droplets and liquid aerosols, is parametrized according to [Kärcher et al. \(2006\)](#).
222 Heterogeneous ice nucleation, including the immersion and deposition modes, is
223 parameterized as a function of temperature- and ice supersaturation-dependent INP
224 concentration ([Hande et al., 2015](#)). The INP concentration due to immersion
225 nucleation is described as the following equation:

$$226 \quad C_{INP}(T_k) = A \times \exp[-B \times (T_k - T_{min})^C] \quad (1)$$

227 where T_k is the ambient temperature in Kelvin; A , B , and C are fitting constants with
228 different values to represent seasonally varying dust INP concentrations. The
229 parameterization for deposition INPs is simply scaled to the diagnosed relative
230 humidity with respect to ice (RH_{ice}):

$$231 \quad C_{INP}(T_k, RH_{ice}) \approx C_{INP}(T_k) \times DSF(RH_{ice}) \quad (2)$$

$$232 \quad DSF(RH_{ice}) = a \times \arctan(b \times (RH_{ice} - 100) + c) + d \quad (3)$$

233 where $C_{INP}(T_k)$ is given by Equation (1); a , b , c , and d are constants. More details
234 are found in [Hande et al. \(2015\)](#).

235 **2.2. Simulation setup and sensitivity experiments**

236 In this study, the setup consists of two different domains with one-way nesting
237 covering a major part of central Europe ([Figure 1](#)). The horizontal resolution for the
238 nested domains is halved from 2400 m to 1200 m in the innermost domain, and the
239 time steps for the two domains are 12 s and 6 s, respectively. 150 vertical levels are
240 used, with a grid stretching towards the model top at 21 km. The vertical resolution is
241 the same for all horizontal resolutions and the lowest 1000 m encompass 20 layers.
242 A 1-D vertical turbulence diffusion and transfer scheme is used for the 2400 m and

243 1200 m resolutions, referred to as numerical weather prediction (NWP) physics.
244 Deep convection is assumed to be explicitly resolved, while shallow convection is
245 parameterized for both domains. The simulations are initialized at 00:00 UTC on the
246 study day from ICON-EU analyses and integrated for 24 hours. Simulation results
247 were saved every 15 minutes. At the lateral boundaries of the outer domain, the
248 simulation of the model is updated with 3-hourly ICON-EU analyses. The nested
249 domains are coupled online, and the outer domain provides lateral boundary
250 conditions to the inner domain.

251

252 In nature, INP concentration varies across multiple orders of magnitude ([Hoose and](#)
253 [Möhler, 2012](#); [Kanji et al., 2017](#)). Thus, in our sensitivity experiments, heterogeneous
254 ice formation was scaled by multiplying the default INP concentration (Equation (1))
255 with a factor of 10^{-2} , 10^{-1} , 10^1 , 10^2 , 10^3 for both immersion freezing and deposition ice
256 nucleation. Together with a case with default INP concentration (case CTRL) and
257 one case switching off the secondary-ice production via rime-splintering process (the
258 so called Hallet-Mossop process), 7 cases were created in total to investigate the
259 impact of primary and secondary ice formation on cloud phase distribution in deep
260 convective clouds.

261

262 In order to assess the sensitivity of the cloud phase to thermodynamics, initial and
263 lateral boundary temperature fields are modified with increasing and decreasing
264 temperature increments, named experiments INC and DEC, respectively. The
265 temperature increment is linearly increased/decreased with height from 0 K at 3 km
266 to +/-3K and +/-5K at 12 km, creating 4 sensitivity experiments DEC03, DEC05,
267 INC03, and INC05. Above 12 km, the increment is constant up to the model top.

268 Initial temperature profiles are shown in [Figure 2](#). The increasing or decreasing
269 environmental temperature leads to changes in the lapse rate and the stability of the
270 atmosphere, and hence results in decrease or increase in the convective available
271 potential energy (CAPE), respectively ([Barthlott and Hoose, 2018](#)). Thus, the CAPE
272 increases monotonically from case INC05 (spatial-averaged CAPE at 9:00 UTC: 413
273 J kg^{-1}) to case CTRL (724 J kg^{-1}) and finally to DEC05 (1235 J kg^{-1}). Note that the
274 relative humidity increases/decreases with decreasing/increasing temperature as the
275 specific humidity is unperturbed. The perturbations of INP concentration and
276 initial/lateral temperature profiles are motivated by [Hoose et al. \(2018\)](#) and [Barthlott](#)

删除了: s

删除了: are

删除了: ing

删除了: ing

删除了: between 3 and

删除了: Figure 2

设置了格式: 字体: 非倾斜

283 [and Hoose \(2018\)](#), respectively. Complementary to these earlier studies, we now
284 investigate an ensemble of several deep convective clouds and focus on influences
285 of INP and thermodynamics on cloud phase distribution. Short descriptions of all
286 sensitivity experiments performed in this study are listed in [Table 1](#).

287 2.3. Satellite observations and retrieval algorithms

288 The Spinning Enhanced Visible and Infrared Imager (SEVIRI) is a 12-channel imager
289 on board the geostationary Meteosat Second Generation (MSG) satellites. SEVIRI
290 has one high spatial resolution visible channel (HRV) and 11 spectral channels from
291 0.6 to 14 μm with a 15 min revisit cycle and a spatial resolution of 3 km at nadir
292 ([Schmetz et al., 2002](#)). Based on the spectral measurements of SEVIRI, a cloud
293 property data record, the CLAAS-2 dataset (CLOUD property dAtAset using SEVIRI,
294 Edition 2), has been generated in the framework of the EUMETSAT Satellite
295 Application Facility on Climate Monitoring (CM SAF) ([Benas et al., 2017](#)). CLAAS-2
296 is the successor of CLAAS-1 ([Stengel et al., 2014](#)), for which retrieval updates have
297 been implemented in the algorithm for the detection of clouds compared to CLAAS-1
298 ([Benas et al., 2017](#)) with the temporal coverage being extended to 2004-2015.
299 Retrieval algorithms for parameters that are important for this study are introduced
300 below. Detailed descriptions for the retrieval algorithms are found in [Stengel et al.](#)
301 [\(2014\)](#) and [Benas et al. \(2017\)](#) with the main features being summarized in the
302 following.

303
304 The MSGv2012 software package is employed to detect clouds and their vertical
305 placement ([Derrien and Le Gléau, 2005](#); [Benas et al., 2017](#)). Multi-spectral threshold
306 tests, which depend on illumination and surface types, among other factors, are
307 performed to detect cloud appearances. Each satellite pixel is assigned to categories
308 of cloud-filled, cloud-free, cloud water contaminated, or snow/ice contaminated.
309 Cloud top pressure (CTP) is retrieved with different approaches using input from
310 SEVIRI channels at 6.2, 7.3, 10.8, 12.0, and 13.4 μm ([Menzel et al., 1983](#); [Schmetz](#)
311 [et al., 1993](#); [Stengel et al., 2014](#); [Benas et al., 2017](#)). Cloud top height (CTH) and
312 cloud top temperature (CTT) are derived from CTP using ancillary data for
313 temperature and humidity profiles from ERA-Interim ([Dee et al., 2011](#)). The cloud top
314 phase (CPH) retrieval is based on a revised version of the multispectral algorithm

删除了: Table 1

设置了格式: 字体颜色: 自动设置

设置了格式: 字体: 非倾斜, 字体颜色: 自动设置, 检查拼写和语法

316 developed by [Pavolonis et al. \(2005\)](#). Clouds are categorized initially into six types,
317 that are liquid, supercooled, opaque ice, cirrus, overlap, and overshooting.
318 Subsequently, the binary cloud phase (liquid or ice) is generated based on the six
319 categories ([Benas et al., 2017](#)). Cloud optical and microphysical properties are
320 retrieved using the Cloud Physical Properties (CPP) algorithm ([Roebeling et al.,
321 2006](#)). SEVIRI visible (0.6 μm) and near-infrared (1.6 μm) measurements are used
322 to calculate cloud optical thickness (COT) and cloud particle effective radius (r_e) by
323 applying the [Nakajima and King \(1990\)](#) approach in the CPP algorithm ([Stengel et
324 al., 2014; Benas et al., 2017](#)). Liquid water path (LWP) and ice water path (IWP) are
325 then computed as a function of liquid/ice water density, COT, and r_e of cloud water
326 and cloud ice following the scheme developed by [Stephens \(1978\)](#).

327
328 In this study we used instantaneous CLAAS-2 data with temporal resolution of 15
329 minutes and on native SEVIRI projection and resolution. In addition to the CLAAS-2
330 dataset, the recently developed software suite SEVIRI_ML ([Philipp and Stengel
331 \(2023\) in preparation; code available on Github:
332 \[https://github.com/danielphilipp/seviri_ml\]\(https://github.com/danielphilipp/seviri_ml\)](#)) was applied to the SEVIRI measurements
333 to obtain cloud top phase and cloud top temperature for the selected case.
334 SEVIRI_ML uses a machine learning approach calibrated against [Cloud-Aerosol
335 Lidar with Orthogonal Polarization \(CALIOP\) data](#). One feature of the SEVIRI_ML is
336 that it also provides pixel-based uncertainties such that values with low reliability can
337 be filtered out. [We applied the retrieval algorithms to the model simulations in this
338 study and compared the results to satellite observations. A similar strategy was used
339 by Kay et al. \(2018\) for the evaluation of precipitation in a climate model with
340 CloudSat observations and termed "scale-aware and definition-aware evaluation".](#)

341 2.4. Satellite forward operators

342 In order to compare simulation results and satellite observations directly, SEVIRI-like
343 spectral reflectance and brightness temperatures are calculated using the radiative
344 transfer model for TOVS (RTTOV, v12.3) ([Saunders et al., 2018](#)). RTTOV is a fast
345 radiative transfer model for simulating top-of-atmosphere radiances from passive
346 visible, infrared, and microwave downward-viewing satellite radiometers. It has been
347 widely used in simulating synthetic satellite images and assimilating radiances in

删除了: Philipp and Stengel,

删除了: to be submitted

删除了:

移动了(插入) [1]

删除了: [Stengel et al. \(2020\)](#) applied a cloud classification algorithm developed for satellite observations to model simulated brightness temperatures in a similar manner.

355 numerical models ([Saunders et al., 2018](#); [Pscheidt et al., 2019](#); [Senf et al., 2020](#);
356 [Geiss et al., 2021](#); [Rybka et al., 2021](#)).

357

358 In this work, ICON simulated surface skin temperature, near-surface pressure,
359 temperature, specific humidity, wind velocity, total liquid water content, total ice water
360 content, and effective radius of cloud liquid and cloud ice are used as input to drive
361 the RTTOV model. Before inputting to the RTTOV model, ICON simulations are
362 remapped onto SEVIRI's full disc coordinate. Brightness temperatures from 8
363 channels (at 3.9, 6.2, 7.3, 8.7, 9.7, 10.8, 12.0, and 13.4 μm) and reflectance from 3
364 channels (at 0.6, 0.8, and 1.6 μm) simulated by the RTTOV model are used as input
365 to run the remote sensing retrieval algorithms to derive CLAAS-2-like and
366 SEVIRI_ML-like retrievals, named ICON_RTTOV_CLAAS-2 and
367 ICON_RTTOV_SEVIRI_ML products, respectively.

368 **2.5. Synoptic overview**

369 The day 06 June 2016 was selected to analyze, which was dominated by
370 summertime deep convection located in central Europe. The synoptic forcing was
371 weak on the day, and convection was triggered mainly by local thermal instabilities.
372 The day has been discussed frequently in previous studies in terms of convection
373 triggering, cloud microphysics, and its parameterizations ([Keil et al., 2019](#); [Geiss et
374 al., 2021](#)).

375 **3. Results and discussion**

376 Perturbing INP concentration and temperature profiles directly affects microphysical
377 and thermodynamic processes of the developing deep convective clouds, and hence
378 impact in-cloud and cloud-top phase distributions. The following section shows
379 results and discussions on the sensitivities of cloud phase and cloud microphysics to
380 INP concentration and thermodynamic perturbations.

381 **3.1. Spatial distribution of cloud properties**

382 Before analyzing the results of sensitivity experiments, retrieved cloud properties via
383 RTTOV and the CLAAS-2 retrieval scheme for the CTRL case are compared to
384 CLAAS-2 products. Spatial distributions of derived LWP, IWP, and COT at 13:00

385 UTC of the CTRL case and CLAAS-2 satellite observation are shown in [Figure 3](#),
386 Discrepancies are found between ICON simulation and CLAAS-2 satellite
387 observations in terms of spatial coverage and intensity. The ICON simulation
388 overestimates the cloud coverage of low-level liquid clouds compared to CLAAS-2
389 satellite observations, while LWP derived from the ICON simulation (case CTRL) is
390 smaller and more homogeneously distributed than that from the CLAAS-2
391 observation ([Figure 3a](#) and [3b](#)). The spatial distributions of IWP and COT represent
392 the approximate location and spatial extension of deep convective clouds in this
393 study. The ICON simulation could reproduce cores of deep convective clouds of a
394 number and spacing comparable to observations, while the spatial extension and
395 intensity of individual deep convective clouds are not simulated very well by the
396 ICON model. The ICON simulation underestimates the spatial extension of deep
397 convective clouds but overestimates IWP and COT outside the convective cores
398 compared to the CLAAS-2 observation ([Figure 3c-f](#)).

删除了: Figure 3

399
400 Overall, the simulated clouds appear to be too homogeneous without sufficient
401 internal structure. [Geiss et al. \(2021\)](#) also reported significant deviations between
402 model simulations and satellite observations. The error sources are manifold and
403 may originate from the model physics as well as from the forward operator and the
404 retrieval algorithm. [Geiss et al. \(2021\)](#) investigated the sensitivity of derived visible
405 and infrared observation equivalents to model physics and operator settings. They
406 found that the uncertainty of the visible forward operator is sufficiently low while
407 infrared channels could bring errors in cloud-top variables. [Geiss et al. \(2021\)](#)
408 concluded that the primary source of deviations is mainly from model physics,
409 especially model assumptions on subgrid-scale clouds. In addition to the subgrid-
410 scale cloud scheme, multiple critical cloud microphysical processes missing from the
411 model, introducing significant uncertainties into the simulation results. For example,
412 entrainment mixing process is not resolved or parameterized in the model, which has
413 essential influences on processes at cloud boundaries and hence the cloud
414 properties ([Mellado, 2017](#)). Moreover, secondary ice processes including droplet
415 shattering and collisional breakup due to ice particles collisions are missing, which
416 have significant impacts on the cloud ice microphysics ([Sullivan et al., 2018](#);
417 [Sotiropoulou et al., 2021](#)).

删除了: Figure 3

设置了格式: 字体: 非倾斜

删除了: Figure 3

删除了: Moreover,

删除了: concluded

423 **3.2. Sensitivity of microphysical properties to INP perturbation**

424 Perturbing INP concentration results in a direct influence on the heterogeneous
425 freezing processes and hence impacts on cloud microphysical properties.
426 Systematic variations have been found in the spatial- and time-averaged profiles of
427 mass mixing ratios of cloud hydrometeors as shown in [Figure 4](#). All profiles
428 discussed here are averaged over cloudy pixels (defined as having a condensed
429 mass of cloud water plus total cloud ice greater than a threshold of $1.0 \times 10^{-5} \text{ kg kg}^{-1}$)
430 and over the time period from 9:00 to 19:00 UTC, when convection was well
431 developed. The mass concentration of ice crystals decreases with increasing INP
432 concentration ([Figure 4a](#)). However, the mass concentration of snow, graupel, and
433 rainwater increase with increasing INP concentration, especially in the high INP
434 concentration cases (cases $A \times 10^2$ and $A \times 10^3$).

435
436 In order to further reveal why ice crystal mass concentration decreases with
437 increasing INP concentration, we investigate process rates related to ice particle
438 nucleation and growth. [Figure 5](#) shows spatial- and time-averaged (from 9:00 to
439 19:00 UTC) profiles of process rates for homogeneous freezing, heterogeneous
440 freezing, secondary ice production via the rime-splintering process, cloud droplets
441 rimed with ice crystals, rain droplets rimed with ice crystals, and collection between
442 ice and ice crystals. Heterogeneous freezing ([Figure 5a](#)) includes processes of
443 immersion freezing, deposition ice nucleation, and immersion freezing of liquid
444 aerosols ([Kärcher et al., 2006](#); [Hande et al., 2015](#)), see also equations (1) and (2).
445 Process rates of heterogeneous freezing increase significantly with increasing INP
446 concentration compared to the CTRL ([Figure 5a](#)). Compensating the change in
447 heterogeneous freezing, process rates of homogeneous freezing decrease
448 significantly with increasing INP concentration ([Figure 5b](#)). However, a decrease in
449 INP concentration (compared to the CTRL) does not have a strong influence on the
450 heterogeneous freezing mass rate, which is already low compared to the other
451 processes in CTRL. Riming processes of cloud droplets and rain droplets onto ice
452 crystals are greatly invigorated due to enhanced INP concentration ([Figure 5d](#) and
453 [5e](#)). Moreover, process rates of secondary ice production due to rime-splintering are
454 strengthened as well due to the increase in rimed ice, albeit much lower values.
455 [Figure 5f](#) shows process rates of collection between ice and ice crystals. Process

删除了: Figure 4

设置了格式: 字体: 非倾斜

删除了: cloud

删除了: Figure 4

设置了格式: 字体: 非倾斜

删除了: Figure 5

设置了格式: 字体: 非倾斜

删除了: Figure 5

设置了格式: 字体: 非倾斜

删除了: Figure 5

设置了格式: 字体: 非倾斜

删除了: Figure 5

设置了格式: 字体: 非倾斜

删除了: Figure 5

删除了: Figure 5

465 rates of collection between ice and ice particles increase with increasing INP
466 concentration, especially in high INP concentration cases (cases $A \times 10^2$ and $A \times 10^3$).
467 Process rates of collection of other ice particles all increase with increasing INP
468 concentration, similar to the collection between ice and ice crystals (not shown). The
469 increase in the riming of clouds and rain droplets onto ice crystals and collections
470 between ice particles leads to the increase in the mass concentration of snow,
471 graupel, and hail (Figure 4b and 4c). However, the total mass increase in snow,
472 graupel, and hail do not outbalance the decrease in the mass concentration of ice
473 crystals (Figure 4). The weakened homogeneous freezing is most likely the dominant
474 factor leading to the decrease in ice mass concentration in high INP cases,
475 considering the magnitude of the process rate of homogeneous freezing (Figure 5b).
476 Supercooled liquid and cloud droplets have been converted into ice crystals before
477 reaching the homogeneous freezing layer, leading to fewer supercooled droplets
478 remaining for homogeneous freezing. Even though homogeneous freezing is
479 weakened in high INP cases, the process rate of homogeneous freezing is still larger
480 than heterogeneous freezing, which means homogeneous freezing is the dominant
481 ice formation process in the convective clouds discussed in this study. Moreover, the
482 enhanced production of large ice particles (snow, graupel, and hail) in the highest
483 INP case, which sediment more rapidly to lower levels, leads to increased surface
484 precipitation by about 10% in the $A \times 10^3$ case (not shown). Interestingly, ice crystal
485 effective radius (r_e^{ice}) increases monotonically with increasing INP concentration,
486 especially in the mixed-phase layer (Figure 4e). Zhao et al. (2019) also reported an
487 increased r_e^{ice} with polluted continental aerosols in their simulated moderate
488 convection cases, and they attributed it to enhanced heterogeneous freezing and
489 prolonged ice crystal growth at higher INP loading.

490
491 This competition between homogeneous and heterogeneous freezing has been
492 discussed in previous studies (Heymsfield et al., 2005; Deng et al., 2018; Takeishi
493 and Storelvmo, 2018). In contrast, simulations of mixed-phase moderately deep
494 convective clouds by Miltenberger and Field (2021) indicate that cloud ice mass
495 concentration increases with increasing INP concentration, which is in opposition to
496 the findings in this work. The main reason is that the CTT is about -18°C in
497 Miltenberger and Field (2021)'s study, and heterogeneous freezing does not

删除了: Figure 4

设置了格式: 字体: 非倾斜

删除了: Figure 4

设置了格式: 字体: 非倾斜

删除了: Figure 5

设置了格式: 字体: 非倾斜

删除了: Figure 4

502 compete with homogeneous freezing. Thus, results on INPs effects on glaciation
503 processes in convective clouds can be opposite under different conditions.

504 3.3. Cloud liquid mass fraction

505 Varying the INP concentration has a direct impact on the primary ice formation.
506 Thus, it affects cloud liquid mass fraction within the clouds (directly for all cloudy
507 layers where heterogeneous freezing is active and indirectly for warmer and colder
508 temperatures) and at the cloud top. Cloud liquid mass fraction is defined as the ratio
509 of mass mixing ratio between cloud droplets (q_c) and the sum of cloud droplets and
510 cloud ice crystals (q_i). In-cloud liquid mass fraction, sampled at a time interval of 15
511 minutes between 9:00 to 19:00 from all cloudy pixels, is shown as scatterplots
512 versus temperature in [Figure 6a-d](#). The corresponding frequencies of the occurrence
513 of the temperature/liquid fraction bins are shown in [Figure 6e-h](#). Similar analyses
514 were made by [Hoose et al. \(2018\)](#), but for idealized simulations of deep convective
515 clouds. In-cloud liquid mass fractions smaller than 0.5 are quite common already at
516 temperature just below $-3\text{ }^\circ\text{C}$ except for the case without rime-splintering process
517 ($A \times 10^0$ _NSIP). The decrease in INP concentrations has limited effects on the in-
518 cloud liquid mass fraction ([Figure 6c](#) and [6g](#)), while a stronger influence has been
519 found in the case with enhanced INP concentration ([Figure 6d](#) and [6h](#)). The number
520 of pixels having high liquid mass fraction values at temperatures lower than $-30\text{ }^\circ\text{C}$
521 decreases with increasing INP concentration. In addition, more and more pixels
522 having liquid mass fraction smaller than 0.5 appear with increasing INP
523 concentration and the number of pure ice pixels increases with increasing INP
524 concentration as well. This is because higher INP concentration intensifies the
525 heterogeneous freezing processes (immersion freezing and deposition ice
526 nucleation) and invigorates the rime-splintering process as well (will be discussed in
527 section 3.4). Interestingly, at the lower end of the mixed-phase temperature range ($-$
528 $38\text{ }^\circ\text{C} \sim -28\text{ }^\circ\text{C}$), there are fewer pixels having high liquid mass fraction in the high INP
529 case, and those remaining are mainly the ones at high vertical velocities (above ~ 10
530 m/s). This is probably because supercooled droplets are more easily frozen in high
531 INP cases and stronger updrafts are needed to offset the Wegener-Begeron-
532 Findeisen process to maintain the supersaturation with respect to water. Switching
533 off the secondary ice production via rime-splintering process, pixels having a liquid

删除了: Figure 6

设置了格式: 字体: 非倾斜

删除了: Figure 6

设置了格式: 字体: 非倾斜

删除了: Figure 6

设置了格式: 字体: 非倾斜

删除了: Figure 6

设置了格式: 字体: 非倾斜

删除了: 3

539 mass fraction smaller than 0.9 are reduced significantly at temperatures between -
540 10 °C and 0 °C (Figure 6b and 6f).

删除了: Figure 6

设置了格式: 字体: 非倾斜

542 At the cloud top (Figure 7), the number of pixels having a liquid mass fraction smaller
543 than 0.5 increases with increasing INP concentration, which is the same as within
544 the clouds. "Cloud top" is defined as the height of the uppermost cloud layer (which
545 has a condensed mass of cloud water plus cloud total cloud ice greater than a
546 threshold of 1.0×10^{-5} kg kg⁻¹) in a pixel column. At the cloud top, the liquid mass
547 fraction has a more polarized distribution, with either large values or small values,
548 and intermediate values are less common than within the clouds. This is because the
549 vertical velocities at the cloud top are significantly smaller compared to that within
550 the cloud, which leads to a more efficient Wegener-Bergeron-Findeisen process at
551 the cloud top.

删除了: Figure 7

设置了格式: 字体: 非倾斜

552 3.4. Liquid cloud pixel fraction

删除了: number

553 Liquid cloud pixel fractions are calculated differently for model simulations and
554 retrieved cloud products. For simulation results, a cloudy pixel having a cloud liquid
555 mass fraction larger than 0.5 is counted as a liquid pixel, otherwise, it is an ice pixel.
556 Both CLAAS-2 and SEVIRI_ML products and the corresponding retrievals derived
557 from ICON simulations by the satellite forward operators (see section 2.4) provide
558 binary cloud phase information (liquid or ice) only. For these data, the liquid cloud
559 pixel fraction is calculated as the ratio between the number of liquid cloud pixels and
560 the sum of all cloudy pixels.

删除了: number

删除了: pixel number fraction

562 Liquid cloud pixel fractions within clouds and at the cloud top are shown in Figure 8.
563 Decrease in INP concentration has limited impacts on the liquid cloud pixel fraction
564 for in-cloud layers. Increase in INP concentration leads to a decrease in liquid cloud
565 pixel fraction but not monotonically (Figure 8a). The decrease in liquid cloud pixel
566 fraction is significant in the highest INP concentration case (case $A \times 10^3$), while
567 decreases in intermediate INP concentration cases (cases $A \times 10^1$ and $A \times 10^2$) are
568 only obvious in temperature ranges from -30 °C to -20 °C and from -15 °C to -5 °C.
569 Moreover, liquid mass fraction decreases monotonically with increasing INP
570 concentration in the temperature range from about -15 to -35 °C both within the cloud

删除了: pixel number fraction

删除了: Figure 8

设置了格式: 字体: 非倾斜

删除了: pixel number fraction

删除了: pixel number fraction

删除了: Figure 8

删除了: pixel number fraction

设置了格式: 字体: 非倾斜

582 and at the cloud top (except for the lowest INP concentrations), and the decreasing
583 trend is more significant at the cloud top compared to within the cloud (not shown).
584 Switching off the rime-splintering process results in an increase in liquid cloud pixel
585 fraction in the temperature range between -10 °C and -3 °C, which is consistent with
586 the strong decrease in pixels of cloud liquid mass fraction lower than 0.9 in the same
587 temperature range (Figure 7b). The temperature at which the liquid cloud pixel
588 fraction equals 0.5 is often termed “glaciation temperature”. The glaciation
589 temperature shifts slightly to a warmer temperature by ~2 °C at the highest INP
590 concentration case (case A×10³, Figure 8a).

591
592 Sensitivities of the cloud phase to INP concentration are more complex at the cloud
593 top than inside the cloud. Liquid cloud pixel fractions at the cloud top calculated
594 directly from ICON simulations on its native grid (~1200 m) are shown in Figure 8b.
595 Cloud-top liquid pixel fraction decreases significantly with increasing INP
596 concentration. In the temperature range between -35 °C and -15 °C, where
597 heterogeneous freezing processes (immersion freezing and deposition nucleation)
598 are dominant, the impact of INP is most pronounced. Above -15 °C, the impact of
599 INP does not disappear, especially in the highest INP concentration case (case
600 A×10³). This is mostly likely due to the sedimentation of ice crystals from upper
601 layers and the secondary ice production invigorated by the Wegener-Begeron-
602 Findeisen process. Switching off the rime-splintering process increases cloud-top
603 liquid pixel fraction only slightly in the temperature range from -10 °C to -3 °C and is
604 almost identical to the control run (case CTRL) outside this temperature range.
605 Interestingly, the shift of glaciation temperature with increasing INP concentration is
606 about 8 °C (Figure 8b) at the cloud top, which is stronger than that inside the clouds
607 (~2 °C, Figure 8a). A possible explanation is that, typically, the vertical velocity at the
608 cloud top is smaller than within the cloud and the ice formation through the Wegener-
609 Bergeron-Findeisen process is expected to be more efficient. Thus, the Wegener-
610 Bergeron-Findeisen process is more sensitive to INP perturbation at the cloud top
611 than within clouds, and leads to the glaciation temperature shifting to be more
612 significant at the cloud top.
613

删除了: pixel number fraction

删除了: Figure 7

删除了: pixel number fraction

设置了格式: 字体: 非倾斜

删除了: Figure 8

删除了: pixel number fraction

删除了: Figure 8

设置了格式: 字体: 非倾斜

删除了: pixel number fraction

删除了: pixel number fraction

删除了: Figure 8

设置了格式: 字体: 非倾斜

删除了: Figure 8

设置了格式: 字体: 非倾斜

624 Liquid cloud pixel fractions at the cloud top calculated directly from ICON simulations
 625 on SEVIRI's grid (~ 5000 m) are shown in Figure 8c. They are noisier and do not
 626 exhibit the small minimum between -10 °C and -3 °C related to rime-splintering, but
 627 are otherwise very similar to Figure 8b. In contrast, the scale-aware and definition-
 628 aware ICON_RTTOV_CLAAS-2 cloud-top liquid pixel fractions shown in Figure 8d
 629 differ markedly from the direct or regridded model output. Above -23 °C, increase
 630 and decrease in INP concentration both lead to a decrease in cloud-top liquid pixel
 631 fraction at certain temperature, but the high INP concentration cases (cases $A \times 10^2$
 632 and $A \times 10^3$), still exhibit the lowest liquid fractions, and case $A \times 10^0$ NSIP the highest.
 633 Thus, the fingerprints of primary and secondary ice formation are retained in the
 634 ICON_RTTOV_CLAAS-2 liquid fraction in this temperature range only for very strong
 635 perturbations. At the same time, it must be noted that the decrease of the liquid pixel
 636 fraction to values around 0.8 above -15 °C is not related to the rime-splintering
 637 process, but to the application of the CLAAS-2 satellite simulator. Below -23 °C, in
 638 the high INP cases $A \times 10^2$ and $A \times 10^3$, cloud-top liquid pixel fractions even increase
 639 with increasing INP concentration. In moderate and low INP cases, the impacts of
 640 INP perturbation are not pronounced. Moreover, the shape of cloud-top liquid pixel
 641 fraction decreasing with cloud-top temperature is different from that in Figure 8b.
 642 Here, the fingerprints of the ice formation processes are completely lost. As
 643 demonstrated in Figure 8c, remapping of simulation data onto SEVIRI's coarser grid
 644 is not the cause of liquid pixel fraction difference between direct ICON output and the
 645 ICON_RTTOV_CLAAS-2 diagnostics, but the CLAAS-2 retrieval algorithm itself is
 646 responsible.

647

648 The satellite observed cloud-top liquid pixel fraction from CLAAS-2 is plotted as a
 649 grey dashed line in Figure 8d. It does not reach 1.0 for all cases even as the cloud-
 650 top temperature is approaching 0 °C, and shows a different temperature dependency
 651 than the simulated curves. No matter how strong the INP concentration and rime-
 652 splintering are perturbed, the retrieved cloud-top liquid pixel fractions from simulation
 653 data deviate strongly from the CLAAS-2 products. In this context one should note
 654 that in particular cloud edges have been found to be problematic situations for the
 655 cloud retrievals, being to some extent responsible for biasing the liquid-pixel fraction
 656 towards smaller values, in particular for the CLAAS-2 data.

删除了: pixel number fraction

删除了: Figure 8

设置了格式: 字体: 非倾斜

删除了: Figure 8

设置了格式: 字体: 非倾斜

删除了: pixel number fraction

删除了: Figure 8

设置了格式: 字体: 非倾斜

删除了: pixel number fraction

删除了: pixel number fraction

删除了: \leftarrow

删除了: pixel number fraction

删除了: pixel number fraction

删除了: Figure 8

设置了格式: 字体: 非倾斜

删除了: Figure 8

设置了格式: 字体: 非倾斜

删除了: pixel number fraction

删除了: loss of information through the postprocessing

设置了格式: 非突出显示

删除了: pixel number fraction

删除了: Figure 8

设置了格式: 字体: 非倾斜

删除了: pixel number fraction

675
676 Finally, the comparison to observations is repeated with the SEVIRI_ML retrieval
677 scheme applied to both simulated radiances (ICON_RTTOV_SEVIRI_ML) and the
678 SEVIRI observations themselves (Figure 8e). As SEVIRI_ML provides uncertainty
679 estimates, pixels for which either the cloud mask uncertainty or the cloud phase
680 uncertainty is larger than 10% are filtered out. While this ensures that only very
681 certain values are kept, it has a significant impact on the number of remaining values
682 as more than 90% of the pixels are filtered out. The resulting liquid pixel fractions
683 ICON_RTTOV_SEVIRI_ML bear a much stronger similarity to the regrided model
684 output in Figure 8c. Remaining differences are a noisier behavior, a plateau of non-
685 zero liquid pixel fractions even below -40 °C, and a general shift to lower
686 temperatures. SEVIRI_ML applied to observations (dashed black line in Figure 8e),
687 with the same uncertainty criterion, exhibits the expected behavior with a liquid
688 fraction of approximately 1 above -10 °C and 0 below approximately -30 °C, and
689 results in a very good agreement to the $A \times 10^3$ case. Generally, the SEVIRI ML
690 retrieval algorithm is assumed to perform better than the CLAAS-2 scheme for both
691 cloud top temperature and cloud phase. This is because SEVIRI ML employs state-
692 of-the-art neural networks to emulate CALIOP v4 data. Moreover, SEVIRI ML
693 provides uncertainty estimates which facilitates fliting out pixels with high
694 uncertainties. Nevertheless, retrieval inaccuracies are unavoidable for passive
695 satellite retrievals which holds true for CLAAS-2 but also for SEVIRI ML.

696 3.5. Sensitivity of cloud phase to atmospheric stability perturbations

697 In addition to the reference run (case CTRL), four cases with perturbations in initial
698 temperatures are analyzed. Mean updraft velocities increase gradually from the low
699 CAPE case INC05 to high CAPE case DEC05 (Figure 9) and cause differences in
700 cloud microphysics and cloud phase distributions.

701
702 In-cloud and cloud-top liquid cloud pixel fractions for the five cases are shown in
703 Figure 10. Systematic shifting of liquid cloud pixel fractions is detected both inside
704 clouds and at the cloud top. Liquid cloud pixel fraction decreases with increasing
705 CAPE from INC05 to DEC05. Both in-cloud and cloud-top glaciation temperatures
706 shift toward warmer temperatures as the CAPE increases, from case INC05 to

删除了: Figure 8

设置了格式: 字体: 非倾斜

删除了: pixel number fraction

删除了: Figure 8

设置了格式: 字体: 非倾斜

删除了: pixel number fraction

删除了: Figure 8

设置了格式: 字体: 非倾斜

删除了: °C

删除了: Figure 9

设置了格式: 字体: 非倾斜

删除了: pixel number fraction

删除了: Figure 10

删除了: pixel number fraction

设置了格式: 字体: 非倾斜

删除了: pixel number fraction

删除了: ing

719 DEC05. This is different from the results reported by [Hoose et al. \(2018\)](#) that cloud-
720 top glaciation temperatures hardly changed with increasing temperature in the
721 boundary-layer by 2 °C, and appears to be contradictory to the expectation that
722 stronger vertical velocities result in a lower glaciation temperature due to
723 suppression of the Wegener-Bergeron-Findeisen process ([Korolev, 2007](#)). Further
724 analysis (not shown) revealed that the mass concentration of cloud ice particle
725 increases while the mass concentration of cloud droplet decreases with the increase
726 in CAPE from case INC05 to DEC05. Moreover, homogeneous and heterogeneous
727 freezing are both enhanced in the high CAPE cases ([Figure 11](#)), possibly due to
728 more transport of moisture to upper levels in the stronger updrafts ([Figure 9](#)). With
729 more ice generated, the Wegener-Bergeron-Findeisen process can be stimulated
730 despite the higher updrafts. Interestingly, cloud-top liquid pixel fractions from the two
731 high CAPE cases (cases DEC03 and DEC05) are closer to SEVIRI observations,
732 both using the CLAAS-2 retrieval ([Figure 10c](#)) and the SEVIRI ML retrieval ([Figure](#)
733 [10d](#)), especially in the temperature range between -10 and -28 °C. Overall,
734 perturbing initial thermodynamic states or CAPE of convective clouds is as important
735 as and may even stronger than the modifications to cloud heterogeneous freezing
736 parameterizations.

737 4. Conclusions

738 Remote sensing products, which cover the entire globe, provide a unique opportunity
739 to constrain the representation of cloud microphysics in global and regional
740 numerical models. In this study, instead of comparing simulation results to satellite
741 observations directly, we derived cloud properties using a radiative transfer model
742 and two different satellite remote sensing retrieval algorithms and then performed the
743 comparison. This enables us to make apples-to-apples comparisons between model
744 simulations and satellite observations. A series of numerical experiments were
745 performed applying convection-permitting simulations with perturbations in INP
746 concentrations and initial thermodynamic states to investigate their impacts on cloud
747 phase distributions in deep convective clouds. Moreover, cloud properties were
748 derived using a satellite forward operator and retrieval algorithms with ICON
749 simulations as input, and compared with CLAAS-2 and SEVIRI ML satellite cloud
750 products to evaluate whether satellite retrievals could detect perturbations in cloud

删除了: Figure 11

删除了: Figure 9

删除了: pixel number fraction

删除了: Figure 10

设置了格式: 字体: 非倾斜

删除了: Figure 10

设置了格式: 字体: 非倾斜

删除了: evaluate cloud microphysical processes of numerical models using satellite observations directly.

758 microphysics and thermodynamics. Uncertainties in the forward operator were
759 however not assessed in this study, which may influence the validity of
760 corresponding results in some extent.

删除了: Simulation results were compared to cloud properties derived from SEVIRI measurements to evaluate the model performance in simulating cloud-top microphysical properties.

761
762 INP concentration was found to have a significant role in shaping cloud phase
763 distributions both within clouds and at the cloud top. Cloud liquid pixel fraction
764 decreased with increasing INP concentration both within the cloud and at the cloud
765 top, indicating a higher glaciation temperature and more intense heterogeneous
766 freezing processes in enhanced INP concentration cases. Interestingly, the
767 influences of INP did not increase linearly but are more pronounced in the high INP
768 concentration cases. In addition, the shifting of glaciation temperature was more
769 significant at the cloud top than within the cloud, which means the impact of INP
770 concentration on cloud phase distribution is more pronounced at the cloud top. It
771 turned out that with the CLAAS-2 retrieval scheme, the INP sensitivity of the cloud-
772 top phase distribution was not detectable, while the SEVIRI_ML retrieval scheme, for
773 which the most uncertain pixels could be excluded, resulted in a better agreement
774 and retained the sensitivity to INP. In contrast, secondary ice production via rime-
775 splintering did not have a detectable impact on the cloud-top phase distribution.
776 Therefore, in future studies, we recommend using the SEVIRI_ML retrieval scheme
777 and SEVIRI_ML satellite-based cloud products.

删除了: pixel number fraction

删除了: s

删除了: do

删除了: i

删除了: This has implications for analyzing cloud products retrieved from passive remote sensing observations. ...

778
779 Ice crystal mass concentration did not increase but decreases with increasing INP
780 concentrations in the simulated deep convective clouds. Process rate analyses
781 revealed that heterogeneous freezing process rates increased with increasing INP
782 concentration, while homogeneous freezing process rates decreased with increasing
783 INP concentration. The competition between heterogeneous freezing and
784 homogeneous freezing for water vapor suppressed ice formation via homogeneous
785 freezing, which was the dominant nucleation process in the simulated deep
786 convective clouds, and hence reduced the cloud ice mass concentration. The
787 increase in heterogeneous nucleation in high INP cases invigorated riming and
788 collection processes of ice particles, making it easier for small ice crystals to grow
789 into large ice aggregates and sediment to lower levels. This was the reason why
790 precipitation increases in enhanced INP cases.

删除了: Total cloud i

删除了: s

删除了: o

删除了: s

删除了: concerns

删除了: s

删除了: i

删除了: decreases

删除了: invigorates

删除了: i

§13 Perturbations in initial thermodynamic states ~~had~~ a strong impact on the cloud phase
§14 distribution both within the cloud and at the cloud top, although the used
§15 perturbations might be rather large compared to initial condition uncertainty in a
§16 weather forecasting context. ~~Moreover, cloud thermodynamics can perturb the cloud~~
§17 ~~phase distribution even stronger than microphysics.~~ To completely distinguish
§18 microphysical impacts from thermodynamic impacts, applying a piggybacking
§19 approach ([Grabowski, 2015](#); [Thomas et al., 2023](#)) in future simulations is necessary.
§20

删除了: have

§21 Utilizing satellite forward operator (the RTTOV radiative model) and remote sensing
§22 retrieval algorithms enabled ~~u~~s to derive cloud-top microphysical ~~propertie~~s and
§23 compare simulation results to satellite products more consistently. However, there
§24 ~~were~~ significant differences in retrieved cloud-top liquid fractions between model
§25 simulations and satellite products. The sources of errors ~~were~~, very complicated and
§26 may come from simulation results, satellite operators, ~~and~~, retrieval algorithms, which
§27 will be investigated in the future. Moreover, the cloud-top property analysis
§28 presented in this study ~~was~~ based on domain-wide statistics, including clouds of
§29 varying types. Statistical results could differ if individual clouds are tracked, as clouds
§30 differ in different experiments in terms of locations and extensions. Although there
§31 are significant uncertainties in satellite forward operators and retrieval algorithms,
§32 passively remote-sensed cloud products provide potential opportunities to constrain
§33 microphysical processes in numerical models.
§34

删除了: roduct

删除了: are

删除了: are

删除了: or

删除了: i

§35 Simulation results of this study revealed a close dependence of heterogeneous
§36 freezing and cloud phase distribution on INP concentrations. Despite this finding, the
§37 ice formation processes in deep convective clouds remain poorly understood. It is
§38 necessary to investigate how and in which conditions the competition of
§39 heterogeneous with homogeneous freezing for water vapor and cloud water depends
§40 on INP availability and vertical velocities in different types of deep convective clouds.
§41 Moreover, the importance of other secondary ice production processes than rime-
§42 splintering (droplet shattering and collisional breakup) in deep convective clouds
§43 need to be quantified in the future.
§44

851 **Competing interests**

852 One of the (co-)authors (Corinna Hoose) is a member of the editorial board of
853 Atmospheric Chemistry and Physics.
854

855 **Acknowledgments**

856 This project has received funding from the European Research Council (ERC) under
857 the European Union's Horizon 2020 research and innovation programme under grant
858 agreement 714062 (ERC Starting Grant "C2Phase"). We gratefully acknowledge the
859 computing time allowed by the German Climate Computing Centre (DKRZ) on the
860 HPC system Mistral and the Steinbuch Centre for Computing (SCC) on the HPC
861 system ForHLR II. The contribution of Martin Stengel was supported by EUMETSAT
862 and its member states through CM SAF.
863

864 **References**

- 865 Barrett, A. I. and Hoose, C.: Microphysical pathways active within thunderstorms and
866 their sensitivity to CCN concentration and wind shear, *Journal of Geophysical*
867 *Research: Atmospheres*, 128, e2022JD036965,
868 <https://doi.org/10.1029/2022JD036965>, 2023.
- 869 Barthlott, C. and Hoose, C.: Aerosol effects on clouds and precipitation over central
870 Europe in different weather regimes, *Journal of the Atmospheric Sciences*, 75,
871 4247-4264, <https://doi.org/10.1175/JAS-D-18-0110.1>, 2018.
- 872 Benas, N., Finkensieper, S., Stengel, M., van Zadelhoff, G. J., Hanschmann, T.,
873 Hollmann, R., and Meirink, J. F.: The MSG-SEVIRI-based cloud property data
874 record CLAAS-2, *Earth Syst. Sci. Data*, 9, 415-434,
875 <http://dx.doi.org/10.5194/essd-9-415-2017>, 2017.
- 876 Bruno, O., Hoose, C., Storelvmo, T., Coopman, Q., and Stengel, M.: Exploring the
877 cloud top phase partitioning in different cloud types using active and passive
878 satellite sensors, *Geophysical Research Letters*, 48, e2020GL089863-
879 e082020GL089863, <https://doi.org/10.1029/2020GL089863>, 2021.
- 880 Coopman, Q., Hoose, C., and Stengel, M.: Analysis of the thermodynamic phase
881 transition of tracked convective clouds based on geostationary satellite
882 observations, *Journal of Geophysical Research: Atmospheres*, 125,
883 e2019JD032146, <https://doi.org/10.1029/2019JD032146>, 2020.
- 884 Coopman, Q., Hoose, C., and Stengel, M.: Analyzing the thermodynamic phase
885 partitioning of mixed phase clouds over the southern ocean using passive
886 satellite observations, *Geophysical Research Letters*, 48, e2021GL093225,
887 <https://doi.org/10.1029/2021GL093225>, 2021.
- 888 Dee, D. P., Uppala, S. M., Simmons, A. J., Berrisford, P., Poli, P., Kobayashi, S.,
889 Andrae, U., Balmaseda, M. A., Balsamo, G., Bauer, P., Bechtold, P., Beljaars,

890 A. C. M., van de Berg, L., Bidlot, J., Bormann, N., Delsol, C., Dragani, R.,
891 Fuentes, M., Geer, A. J., Haimberger, L., Healy, S. B., Hersbach, H., Hólm, E.
892 V., Isaksen, I., Kållberg, P., Köhler, M., Matricardi, M., McNally, A. P., Monge-
893 Sanz, B. M., Morcrette, J. J., Park, B. K., Peubey, C., de Rosnay, P.,
894 Tavolato, C., Thépaut, J. N., and Vitart, F.: The ERA-Interim reanalysis:
895 configuration and performance of the data assimilation system, *Quarterly*
896 *Journal of the Royal Meteorological Society*, 137, 553-597,
897 <https://doi.org/10.1002/qj.828>, 2011.

898 Deng, X., Xue, H., and Meng, Z.: The effect of ice nuclei on a deep convective cloud
899 in South China, *Atmospheric Research*, 206, 1-12,
900 <https://doi.org/10.1016/j.atmosres.2018.02.013>, 2018.

901 Derrien, M. and Le Gléau, H.: MSG/SEVIRI cloud mask and type from SAFNWC,
902 *International Journal of Remote Sensing*, 26, 4707-4732,
903 <https://doi.org/10.1080/01431160500166128>, 2005.

904 Fan, J., Comstock, J. M., and Ovchinnikov, M.: The cloud condensation nuclei and
905 ice nuclei effects on tropical anvil characteristics and water vapor of the
906 tropical tropopause layer, *Environmental Research Letters*, 5, 044005,
907 <https://doi.org/10.1088/1748-9326/5/4/044005>, 2010.

908 Fan, J., Wang, Y., Rosenfeld, D., and Liu, X.: Review of aerosol–cloud interactions:
909 Mechanisms, significance, and challenges, *Journal of the Atmospheric*
910 *Sciences*, 73, 4221-4252, <https://doi.org/10.1175/JAS-D-16-0037.1>, 2016.

911 Field, P. R., Hogan, R. J., Brown, P. R. A., Illingworth, A. J., Choulaton, T. W., Kaye,
912 P. H., Hirst, E., and Greenaway, R.: Simultaneous radar and aircraft
913 observations of mixed-phase cloud at the 100 m scale, *Quarterly Journal of*
914 *the Royal Meteorological Society*, 130, 1877-1904,
915 <https://doi.org/10.1256/qj.03.102>, 2004.

916 Gassmann, A. and Herzog, H.-J.: Towards a consistent numerical compressible non-
917 hydrostatic model using generalized Hamiltonian tools, *Quarterly Journal of*
918 *the Royal Meteorological Society*, 134, 1597-1613,
919 <http://dx.doi.org/10.1002/qj.297>, 2008.

920 Geiss, S., Scheck, L., de Lozar, A., and Weissmann, M.: Understanding the model
921 representation of clouds based on visible and infrared satellite observations,
922 *Atmos. Chem. Phys.*, 21, 12273-12290, [https://doi.org/10.5194/acp-21-12273-](https://doi.org/10.5194/acp-21-12273-2021)
923 [2021](https://doi.org/10.5194/acp-21-12273-2021), 2021.

924 Grabowski, W. W.: Untangling microphysical impacts on deep convection applying a
925 novel modeling methodology, *Journal of the Atmospheric Sciences*, 72, 2446-
926 2464, <https://doi.org/10.1175/JAS-D-14-0307.1>, 2015.

927 Grabowski, W. W., Morrison, H., Shima, S.-I., Abade, G. C., Dziekan, P., and
928 Pawlowska, H.: Modeling of cloud microphysics: Can we do better?, *Bulletin*
929 *of the American Meteorological Society*, 100, 655-672,
930 <https://doi.org/10.1175/BAMS-D-18-0005.1>, 2019.

931 Hande, L. B., Engler, C., Hoose, C., and Tegen, I.: Seasonal variability of Saharan
932 desert dust and ice nucleating particles over Europe, *Atmos. Chem. Phys.*,
933 15, 4389-4397, <http://dx.doi.org/10.5194/acp-15-4389-2015>, 2015.

934 Hande, L. B., Engler, C., Hoose, C., and Tegen, I.: Parameterizing cloud
935 condensation nuclei concentrations during HOPE, *Atmos. Chem. Phys.*, 16,
936 12059-12079, <http://dx.doi.org/10.5194/acp-16-12059-2016>, 2016.

937 Hawker, R. E., Miltenberger, A. K., Wilkinson, J. M., Hill, A. A., Shipway, B. J., Cui,
938 Z., Cotton, R. J., Carslaw, K. S., Field, P. R., and Murray, B. J.: The
939 temperature dependence of ice-nucleating particle concentrations affects the

940 radiative properties of tropical convective cloud systems, *Atmos. Chem.*
 941 *Phys.*, 21, 5439-5461, <https://doi.org/10.5194/acp-21-5439-2021>, 2021.
 942 Heymsfield, A. J., Miloshevich, L. M., Schmitt, C., Bansemer, A., Twohy, C., Poellot,
 943 M. R., Fridlind, A., and Gerber, H.: Homogeneous ice nucleation in subtropical
 944 and tropical convection and its influence on cirrus anvil microphysics, *Journal*
 945 *of the Atmospheric Sciences*, 62, 41-64, <http://dx.doi.org/10.1175/JAS-3360.1>,
 946 2005.
 947 Hoose, C. and Möhler, O.: Heterogeneous ice nucleation on atmospheric aerosols: a
 948 review of results from laboratory experiments, *Atmos. Chem. Phys.*, 12, 9817-
 949 9854, <https://doi.org/10.5194/acp-12-9817-2012>, 2012.
 950 Hoose, C., Karrer, M., and Barthlott, C.: Cloud top phase distributions of simulated
 951 deep convective clouds, *Journal of Geophysical Research: Atmospheres*,
 952 123, 10,410-464,476, <https://doi.org/10.1029/2018JD028381>, 2018.
 953 Kanji, Z. A., Ladino, L. A., Wex, H., Boose, Y., Burkert-Kohn, M., Cziczo, D. J., and
 954 Krämer, M.: Overview of ice nucleating particles, *Meteorological Monographs*,
 955 58, 1.1-1.33, <https://doi.org/10.1175/AMSMONOGRAPHIS-D-16-0006.1>, 2017.
 956 Kärcher, B., Hendricks, J., and Lohmann, U.: Physically based parameterization of
 957 cirrus cloud formation for use in global atmospheric models, *Journal of*
 958 *Geophysical Research: Atmospheres*, 111,
 959 <https://doi.org/10.1029/2005JD006219>, 2006.
 960 Kay, J. E., L'Ecuyer, T., Pendergrass, A., Chepfer, H., Guzman, R., and Yettella, V.:
 961 Scale-aware and definition-aware evaluation of modeled near-surface
 962 precipitation frequency using CloudSat observations, *Journal of Geophysical*
 963 *Research: Atmospheres*, 123, 4294-4309,
 964 <https://doi.org/10.1002/2017JD028213>, 2018.
 965 Keil, C., Baur, F., Bachmann, K., Rasp, S., Schneider, L., and Barthlott, C.: Relative
 966 contribution of soil moisture, boundary-layer and microphysical perturbations
 967 on convective predictability in different weather regimes, *Quarterly Journal of*
 968 *the Royal Meteorological Society*, 145, 3102-3115,
 969 <https://doi.org/10.1002/qj.3607>, 2019.
 970 Korolev, A. and Isaac, G. A.: Relative humidity in liquid, mixed-phase, and ice
 971 clouds, *Journal of the Atmospheric Sciences*, 63, 2865-2880,
 972 <https://doi.org/10.1175/JAS3784.1>, 2006.
 973 Korolev, A.: Limitations of the Wegener–Bergeron–Findeisen mechanism in the
 974 evolution of mixed-phase clouds, *Journal of the Atmospheric Sciences*, 64,
 975 3372-3375, <http://dx.doi.org/10.1175/JAS4035.1>, 2007.
 976 Korolev, A., McFarquhar, G., Field, P. R., Franklin, C., Lawson, P., Wang, Z.,
 977 Williams, E., Abel, S. J., Axisa, D., Borrmann, S., Crosier, J., Fugal, J.,
 978 Krämer, M., Lohmann, U., Schlenker, O., Schnaiter, M., and Wendisch, M.:
 979 Mixed-phase clouds: Progress and challenges, *Meteorological Monographs*,
 980 58, 5.1-5.50, <https://doi.org/10.1175/AMSMONOGRAPHIS-D-17-0001.1>, 2017.
 981 Korolev, A. V., Isaac, G. A., Cober, S. G., Strapp, J. W., and Hallett, J.:
 982 Microphysical characterization of mixed-phase clouds, *Quarterly Journal of*
 983 *the Royal Meteorological Society*, 129, 39-65,
 984 <https://doi.org/10.1256/qj.01.204>, 2003.
 985 Li, R. and Min, Q. L.: Impacts of mineral dust on the vertical structure of precipitation,
 986 *Journal of Geophysical Research: Atmospheres*, 115,
 987 <https://doi.org/10.1029/2009JD011925>, 2010.
 988 Li, X., Tao, W.-K., Masunaga, H., Masunaga, Gu, G., and Zeng, X.: Aerosol effects
 989 on cumulus congestus population over the tropical acific: A cloud-resolving

990 modeling study, *Journal of the Meteorological Society of Japan*, 91, 817-833,
991 10.2151/jmsj.2013-607, 2013.

992 Lohmann, U. and Hoose, C.: Sensitivity studies of different aerosol indirect effects in
993 mixed-phase clouds, *Atmos. Chem. Phys.*, 9, 8917-8934,
994 <https://doi.org/10.5194/acp-9-8917-2009>, 2009.

995 Matus, A. V. and L'Ecuyer, T. S.: The role of cloud phase in Earth's radiation budget,
996 *Journal of Geophysical Research: Atmospheres*, 122, 2559-2578,
997 <https://doi.org/10.1002/2016JD025951>, 2017.

998 McCoy, D. T., Tan, I., Hartmann, D. L., Zelinka, M. D., and Storelvmo, T.: On the
999 relationships among cloud cover, mixed-phase partitioning, and planetary
1000 albedo in GCMs, *Journal of Advances in Modeling Earth Systems*, 8, 650-668,
1001 <https://doi.org/10.1002/2015MS000589>, 2016.

1002 Mecikalski, J. R., Jewett, C. P., Apke, J. M., and Carey, L. D.: Analysis of Cumulus
1003 Cloud Updrafts as Observed with 1-Min Resolution Super Rapid Scan GOES
1004 Imagery, *Monthly Weather Review*, 144, 811-830,
1005 <https://doi.org/10.1175/MWR-D-14-00399.1>, 2016.

1006 Mellado, J. P.: Cloud-top entrainment in stratocumulus clouds, *Annual Review of*
1007 *Fluid Mechanics*, 49, 145-169, 10.1146/annurev-fluid-010816-060231, 2017.

1008 Menzel, W. P., Smith, W. L., and Stewart, T. R.: Improved cloud motion wind vector
1009 and altitude assignment using VAS, *Journal of Applied Meteorology and*
1010 *Climatology*, 22, 377-384, [https://doi.org/10.1175/1520-0450\(1983\)022<0377:ICMWVA>2.0.CO;2](https://doi.org/10.1175/1520-0450(1983)022<0377:ICMWVA>2.0.CO;2), 1983.

1011 Miltenberger, A. K. and Field, P. R.: Sensitivity of mixed-phase moderately deep
1012 convective clouds to parameterizations of ice formation – an ensemble
1013 perspective, *Atmos. Chem. Phys.*, 21, 3627-3642,
1014 <http://dx.doi.org/10.5194/acp-21-3627-2021>, 2021.

1015 Min, Q. L., Li, R., Lin, B., Joseph, E., Wang, S., Hu, Y., Morris, V., and Chang, F.:
1016 Evidence of mineral dust altering cloud microphysics and precipitation,
1017 *Atmospheric Chemistry and Physics*, 9, 3223-3231,
1018 <https://doi.org/10.5194/acp-9-3223-2009>, 2009.

1019 Nakajima, T. and King, M. D.: Determination of the optical thickness and effective
1020 particle radius of clouds from reflected solar radiation measurements. Part I:
1021 Theory, *Journal of Atmospheric Sciences*, 47, 1878-1893,
1022 [https://doi.org/10.1175/1520-0469\(1990\)047<1878:DOTOTA>2.0.CO;2](https://doi.org/10.1175/1520-0469(1990)047<1878:DOTOTA>2.0.CO;2), 1990.

1023 Noh, Y.-J., Seaman, C. J., Vonder Haar, T. H., and Liu, G.: In situ aircraft
1024 measurements of the vertical distribution of liquid and ice water content in
1025 midlatitude mixed-phase clouds, *Journal of Applied Meteorology and*
1026 *Climatology*, 52, 269-279, <https://doi.org/10.1175/JAMC-D-11-0202.1>, 2013.

1027 Pavolonis, M. J., Heidinger, A. K., and Uttal, T.: Daytime global cloud typing from
1028 AVHRR and VIIRS: Algorithm description, validation, and comparisons,
1029 *Journal of Applied Meteorology*, 44, 804-826,
1030 <https://doi.org/10.1175/JAM2236.1>, 2005.

1031 Pinto, J. O.: Autumnal mixed-phase cloudy boundary layers in the Arctic, *Journal of*
1032 *the Atmospheric Sciences*, 55, 2016-2038, [https://doi.org/10.1175/1520-0469\(1998\)055<2016:AMPCBL>2.0.CO;2](https://doi.org/10.1175/1520-0469(1998)055<2016:AMPCBL>2.0.CO;2), 1998.

1033 Pscheidt, I., Senf, F., Heinze, R., Deneke, H., Trömel, S., and Hohenegger, C.: How
1034 organized is deep convection over Germany?, *Quarterly Journal of the Royal*
1035 *Meteorological Society*, 145, 2366-2384, <http://dx.doi.org/10.1002/qj.3552>,
1036 2019.

1039 Roebeling, R. A., Feijt, A. J., and Stammes, P.: Cloud property retrievals for climate
 1040 monitoring: Implications of differences between Spinning Enhanced Visible
 1041 and Infrared Imager (SEVIRI) on METEOSAT-8 and Advanced Very High
 1042 Resolution Radiometer (AVHRR) on NOAA-17, *Journal of Geophysical
 1043 Research: Atmospheres*, 111, <https://doi.org/10.1029/2005JD006990>, 2006.
 1044 Rosenfeld, D. and Woodley, W. L.: Deep convective clouds with sustained
 1045 supercooled liquid water down to -37.5 °C, *Nature*, 405, 440-442,
 1046 <https://doi.org/10.1038/35013030>, 2000.
 1047 Rosenfeld, D., Yu, X., Liu, G., Xu, X., Zhu, Y., Yue, Z., Dai, J., Dong, Z., Dong, Y.,
 1048 and Peng, Y.: Glaciation temperatures of convective clouds ingesting desert
 1049 dust, air pollution and smoke from forest fires, *Geophysical Research Letters*,
 1050 38, <https://doi.org/10.1029/2011GL049423>, 2011.
 1051 Rybka, H., Burkhardt, U., Köhler, M., Arka, I., Bugliaro, L., Górsdorf, U., Horváth, Á.,
 1052 Meyer, C. I., Reichardt, J., Seifert, A., and Strandgren, J.: The behavior of
 1053 high-CAPE (convective available potential energy) summer convection in
 1054 large-domain large-eddy simulations with ICON, *Atmos. Chem. Phys.*, 21,
 1055 4285-4318, <http://dx.doi.org/10.5194/acp-21-4285-2021>, 2021.
 1056 Saunders, R., Hocking, J., Turner, E., Rayer, P., Rundle, D., Brunel, P., Vidot, J.,
 1057 Roquet, P., Matricardi, M., Geer, A., Bormann, N., and Lupu, C.: An update on
 1058 the RTTOV fast radiative transfer model (currently at version 12), *Geosci.
 1059 Model Dev.*, 11, 2717-2737, <http://dx.doi.org/10.5194/gmd-11-2717-2018>,
 1060 2018.
 1061 Schmetz, J., Holmlund, K., Hoffman, J., Strauss, B., Mason, B., Gaertner, V., Koch,
 1062 A., and Van De Berg, L.: Operational cloud-motion winds from meteosat
 1063 infrared images, *Journal of Applied Meteorology and Climatology*, 32, 1206-
 1064 1225, [https://doi.org/10.1175/1520-
 1065 0450\(1993\)032<1206:OCMWFM>2.0.CO;2](https://doi.org/10.1175/1520-0450(1993)032<1206:OCMWFM>2.0.CO;2), 1993.
 1066 Schmetz, J., Pili, P., Tjemkes, S., Just, D., Kerkmann, J., Rota, S., and Ratier, A.: An
 1067 introduction to meteosat second generation (MSG), *Bulletin of the American
 1068 Meteorological Society*, 83, 977-992, [http://dx.doi.org/10.1175/1520-
 1069 0477\(2002\)083<0977:AITMSG>2.3.CO;2](http://dx.doi.org/10.1175/1520-0477(2002)083<0977:AITMSG>2.3.CO;2), 2002.
 1070 Seifert, A. and Beheng, K. D.: A two-moment cloud microphysics parameterization
 1071 for mixed-phase clouds. Part 1: Model description, *Meteorology and
 1072 Atmospheric Physics*, 92, 45-66, [http://dx.doi.org/10.1007/s00703-005-0112-
 1073 4](http://dx.doi.org/10.1007/s00703-005-0112-4), 2006.
 1074 Senf, F., Voigt, A., Clerbaux, N., Hünerbein, A., and Deneke, H.: Increasing
 1075 resolution and resolving convection improve the simulation of cloud-radiative
 1076 effects over the North Atlantic, *Journal of Geophysical Research:
 1077 Atmospheres*, 125, e2020JD032667, <https://doi.org/10.1029/2020JD032667>,
 1078 2020.
 1079 Sheffield, A. M., Saleeby, S. M., and van den Heever, S. C.: Aerosol-induced
 1080 mechanisms for cumulus congestus growth, *Journal of Geophysical
 1081 Research: Atmospheres*, 120, 8941-8952,
 1082 <https://doi.org/10.1002/2015JD023743>, 2015.
 1083 Sotiropoulou, G., Vignon, É., Young, G., Morrison, H., O'Shea, S. J., Lachlan-Cope,
 1084 T., Berne, A., and Nenes, A.: Secondary ice production in summer clouds
 1085 over the Antarctic coast: an underappreciated process in atmospheric models,
 1086 *Atmos. Chem. Phys.*, 21, 755-771, <https://doi.org/10.5194/acp-21-755-2021>,
 1087 2021.

1088 Stengel, M., Kniffka, A., Meirink, J. F., Lockhoff, M., Tan, J., and Hollmann, R.:
 1089 CLAAAS: the CM SAF cloud property data set using SEVIRI, *Atmos. Chem.*
 1090 *Phys.*, 14, 4297-4311, <http://dx.doi.org/10.5194/acp-14-4297-2014>, 2014.
 1091 Stephens, G. L.: Radiation profiles in extended water clouds. II: Parameterization
 1092 schemes, *Journal of Atmospheric Sciences*, 35, 2123-2132,
 1093 [https://doi.org/10.1175/1520-0469\(1978\)035<2123:RPIEWC>2.0.CO;2](https://doi.org/10.1175/1520-0469(1978)035<2123:RPIEWC>2.0.CO;2), 1978.
 1094 Stith, J. L., Haggerty, J. A., Heymsfield, A., and Grainger, C. A.: Microphysical
 1095 characteristics of tropical updrafts in clean conditions, *Journal of Applied*
 1096 *Meteorology*, 43, 779-794, <https://doi.org/10.1175/2104.1>, 2004.
 1097 Sullivan, S. C., Barthlott, C., Crosier, J., Zhukov, I., Nenes, A., and Hoose, C.: The
 1098 effect of secondary ice production parameterization on the simulation of a cold
 1099 frontal rainband, *Atmos. Chem. Phys.*, 18, 16461-16480,
 1100 <https://doi.org/10.5194/acp-18-16461-2018>, 2018.
 1101 Takeishi, A. and Storelvmo, T.: A study of enhanced heterogeneous ice nucleation in
 1102 simulated deep convective clouds observed during DC3, *Journal of*
 1103 *Geophysical Research: Atmospheres*, 123, 13,396-313,420,
 1104 <https://doi.org/10.1029/2018JD028889>, 2018.
 1105 Taylor, J. W., Choullarton, T. W., Blyth, A. M., Liu, Z., Bower, K. N., Crosier, J.,
 1106 Gallagher, M. W., Williams, P. I., Dorsey, J. R., Flynn, M. J., Bennett, L. J.,
 1107 Huang, Y., French, J., Korolev, A., and Brown, P. R. A.: Observations of cloud
 1108 microphysics and ice formation during COPE, *Atmos. Chem. Phys.*, 16, 799-
 1109 826, <https://doi.org/10.5194/acp-16-799-2016>, 2016.
 1110 Thomas, J., Barrett, A., and Hoose, C.: Temperature and cloud condensation nuclei
 1111 (CCN) sensitivity of orographic precipitation enhanced by a mixed-phase
 1112 seeder-feeder mechanism: a case study for the 2015 Cumbria flood, *Atmos.*
 1113 *Chem. Phys.*, 23, 1987-2002, [10.5194/acp-23-1987-2023](https://doi.org/10.5194/acp-23-1987-2023), 2023.
 1114 Twohy, C. H.: Measurements of Saharan dust in convective clouds over the tropical
 1115 eastern Atlantic ocean, *Journal of the Atmospheric Sciences*, 72, 75-81,
 1116 <https://doi.org/10.1175/JAS-D-14-0133.1>, 2015.
 1117 van den Heever, S. C., Carrió, G. G., Cotton, W. R., DeMott, P. J., and Prenni, A. J.:
 1118 Impacts of nucleating aerosol on Florida storms. Part I: Mesoscale
 1119 simulations, *Journal of the Atmospheric Sciences*, 63, 1752-1775,
 1120 <https://doi.org/10.1175/JAS3713.1>, 2006.
 1121 Vignon, É., Alexander, S. P., DeMott, P. J., Sotiropoulou, G., Gerber, F., Hill, T. C.
 1122 J., Marchand, R., Nenes, A., and Berne, A.: Challenging and improving the
 1123 simulation of mid-level mixed-phase clouds over the high-latitude southern
 1124 ocean, *Journal of Geophysical Research: Atmospheres*, 126,
 1125 e2020JD033490, <https://doi.org/10.1029/2020JD033490>, 2021.
 1126 Wan, H., Giorgetta, M. A., Zängl, G., Restelli, M., Majewski, D., Bonaventura, L.,
 1127 Fröhlich, K., Reinert, D., Ripodas, P., Kornblueh, L., and Förstner, J.: The
 1128 ICON-1.2 hydrostatic atmospheric dynamical core on triangular grids – Part 1:
 1129 Formulation and performance of the baseline version, *Geosci. Model Dev.*, 6,
 1130 735-763, <http://dx.doi.org/10.5194/gmd-6-735-2013>, 2013.
 1131 Zängl, G., Reinert, D., Ripodas, P., and Baldauf, M.: The ICON (ICOsahedral Non-
 1132 hydrostatic) modelling framework of DWD and MPI-M: Description of the non-
 1133 hydrostatic dynamical core, *Quarterly Journal of the Royal Meteorological*
 1134 *Society*, 141, 563-579, <http://dx.doi.org/10.1002/qj.2378>, 2015.
 1135 Zhao, B., Wang, Y., Gu, Y., Liou, K.-N., Jiang, J. H., Fan, J., Liu, X., Huang, L., and
 1136 Yung, Y. L.: Ice nucleation by aerosols from anthropogenic pollution, *Nature*
 1137 *Geoscience*, 12, 602-607, <https://doi.org/10.1038/s41561-019-0389-4>, 2019.

1138 Zhao, X., Liu, X., Burrows, S. M., and Shi, Y.: Effects of marine organic aerosols as
1139 sources of immersion-mode ice-nucleating particles on high-latitude mixed-
1140 phase clouds, *Atmos. Chem. Phys.*, 21, 2305-2327,
1141 <https://doi.org/10.5194/acp-21-2305-2021>, 2021.
1142

1143 **Tables:**

1144

1145 Table 1: Setups of simulations performed in this study.

Num	Experiment	Description
1	$A \times 10^0$ (CTRL)	Without any perturbations, the CTRL run, used as a reference.
2	$A \times 10^{-2}$	INP concentrations for both immersion and deposition mode are scaled by multiplying parameter A in Equation (1) by 10^{-2} .
3	$A \times 10^{-1}$	Same as num. 2, but multiplying by 10^{-1} .
4	$A \times 10^1$	Same as num. 2, but multiplying by 10^1 .
5	$A \times 10^2$	Same as num. 2, but multiplying by 10^2 .
6	$A \times 10^3$	Same as num. 2, but multiplying by 10^3 .
7	$A \times 10^0$ _NSIP	INP concentration as in CTRL. The secondary ice production (rime-splintering process) is switched off.
8	DEC05	Initial and lateral temperature decreases from 3 to 12 km with a maximum increment of 5 K. No perturbations in INPs ($A \times 10^0$).
9	DEC03	Same as num. 8, but with a maximum increment of 3 K.
10	INC03	Initial and lateral temperature increases from 3 to 12 km with a maximum increment of 3 K. No perturbations in INPs ($A \times 10^0$).
11	INC05	Same as num. 10, but with a maximum increment of 5 K.

1146

1147

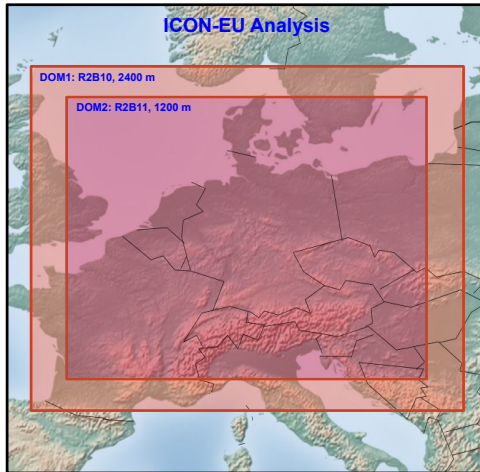
1148

1149

1150 **Figures:**

1151

1152

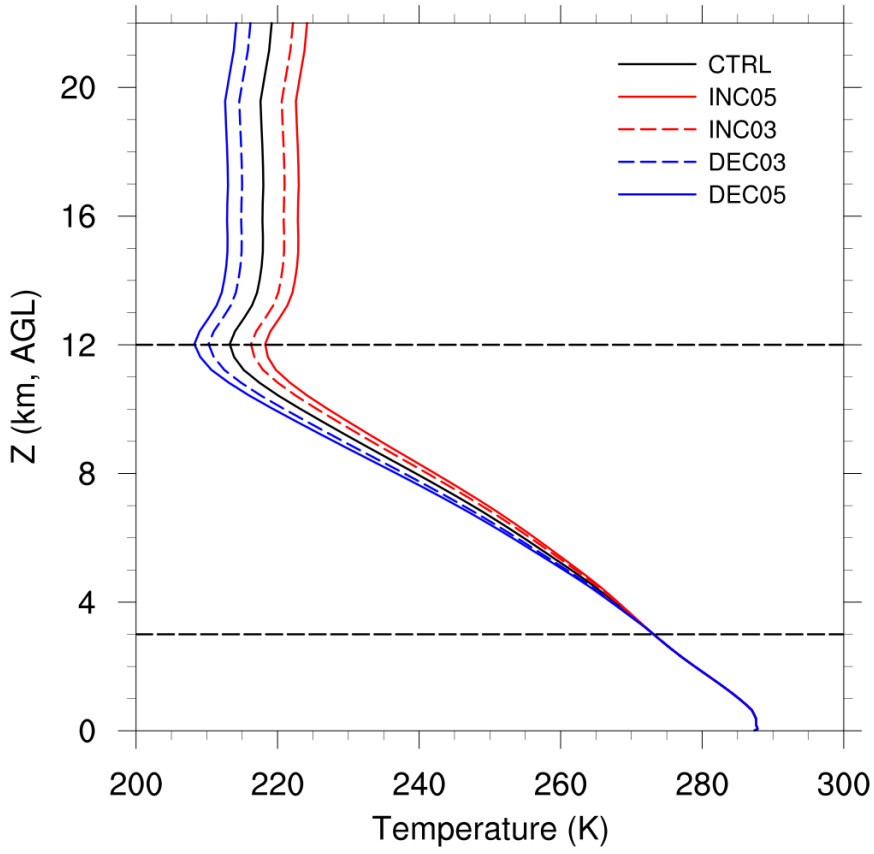


1153

1154 Figure 1: The simulation domains.

1155

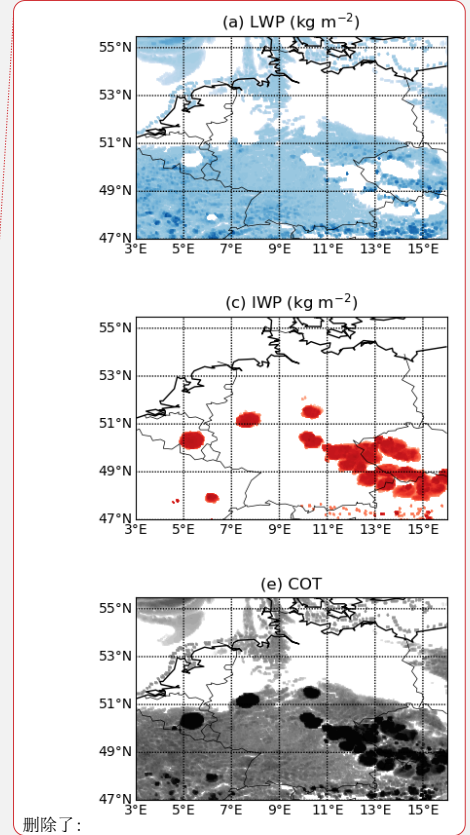
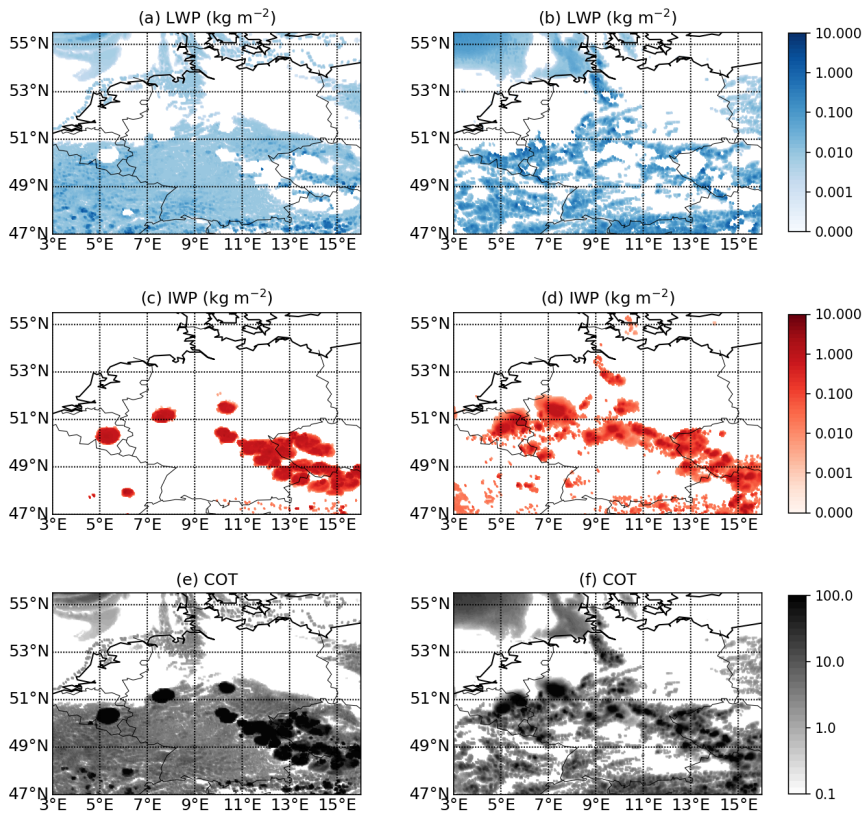
1156



1157

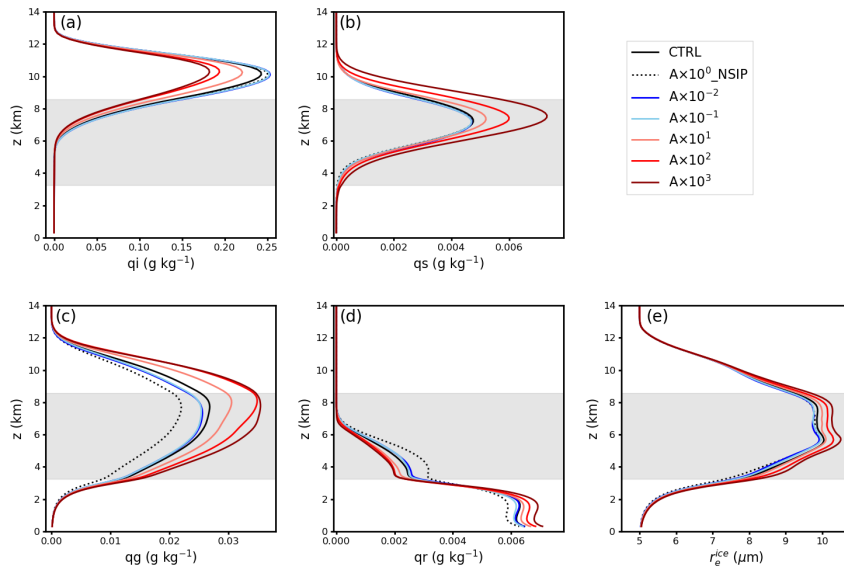
1158 Figure 2: Domain averaged initial temperature profiles. The same modification was
1159 applied to the lateral boundary conditions.

1160



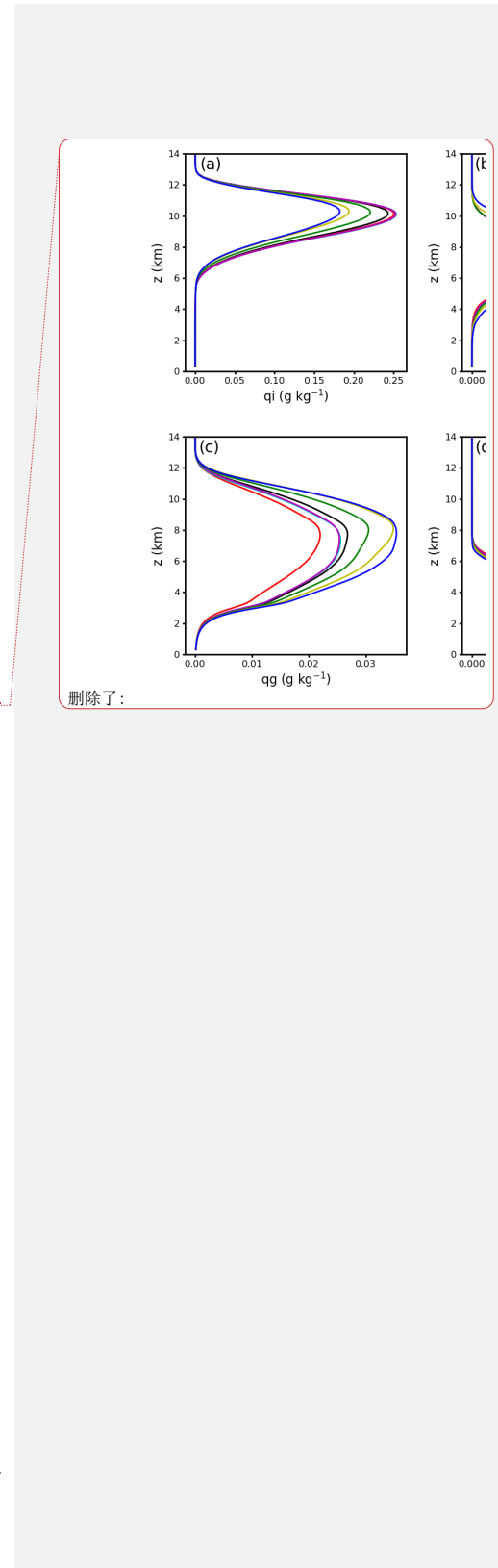
1161
 1162 Figure 3: Spatial distributions of retrieved cloud liquid water path (LWP), ice water
 1163 path (IWP), and cloud optical thickness (COT) at 13:00 UTC. The left panel is for the
 1164 CTRL case (a, c, e) and the right panel is for the CLAAS-2 product (b, d, f).

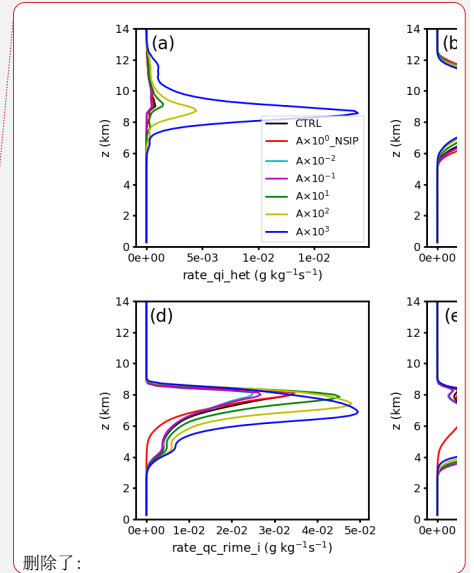
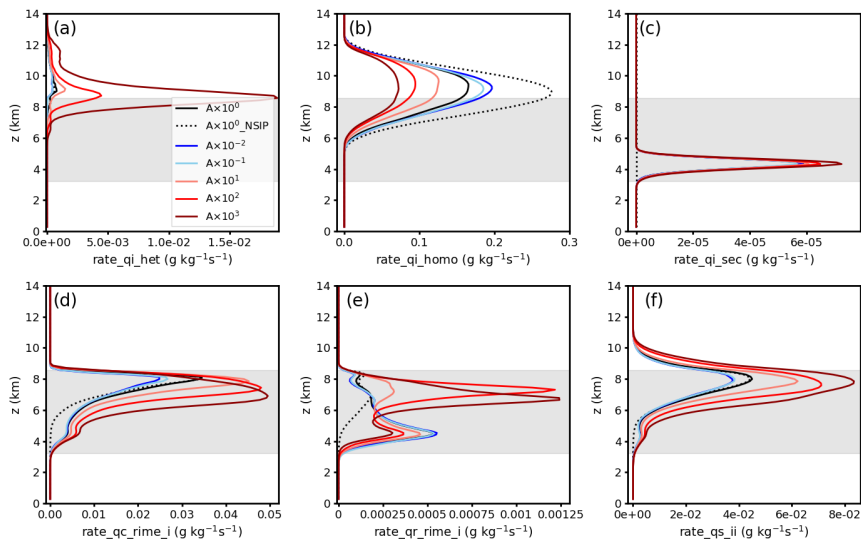
1165



1167
 1168
 1169
 1170
 1171
 1172
 1173

Figure 4: Spatial- and time-averaged (9:00~19:00) profiles of cloud mass mixing ratios of (a) ice crystals, (b) snow, (c) graupel, (d) rainwater, and (e) ice crystal effective radius. Mass mixing ratio unit is g kg^{-1} and the unit of ice crystal effective radius is μm . Shaded area indicates the spatial- and time-averaged mixed-phase region.





删除了:

1175

1176

1177

1178

1179

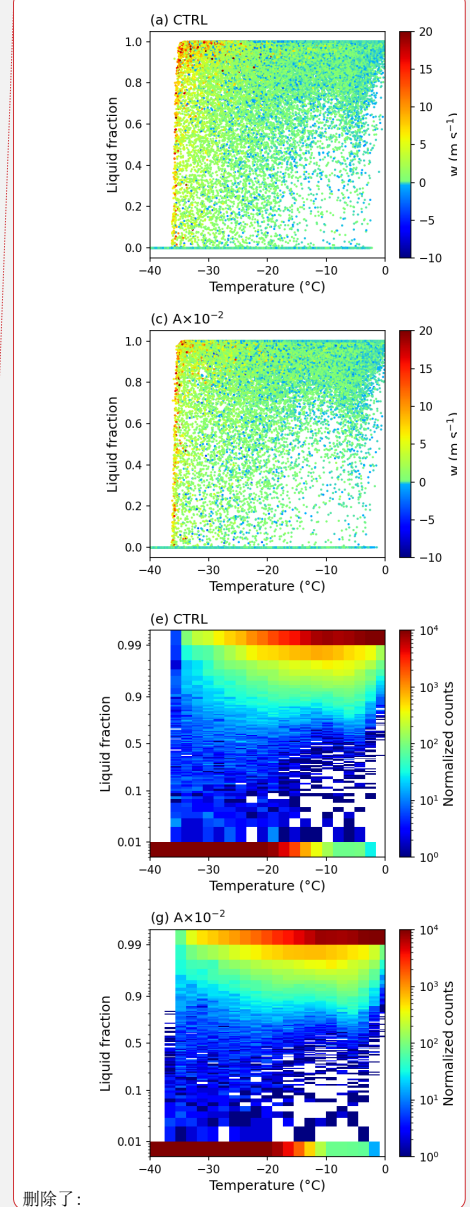
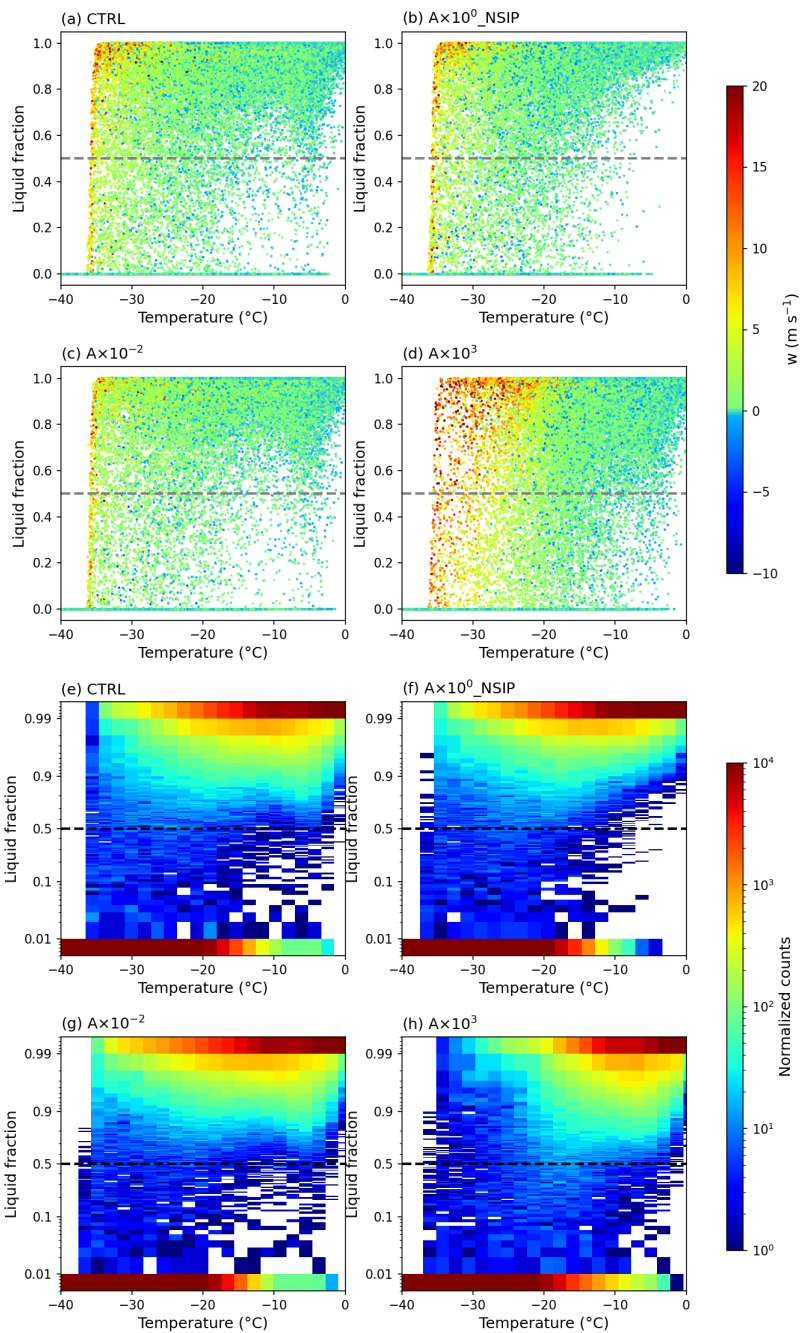
1180

1181

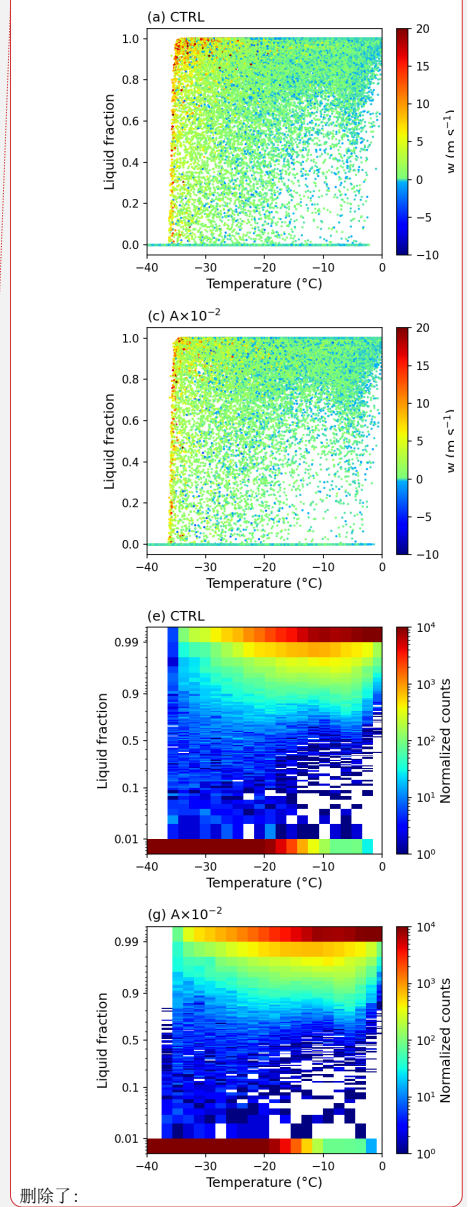
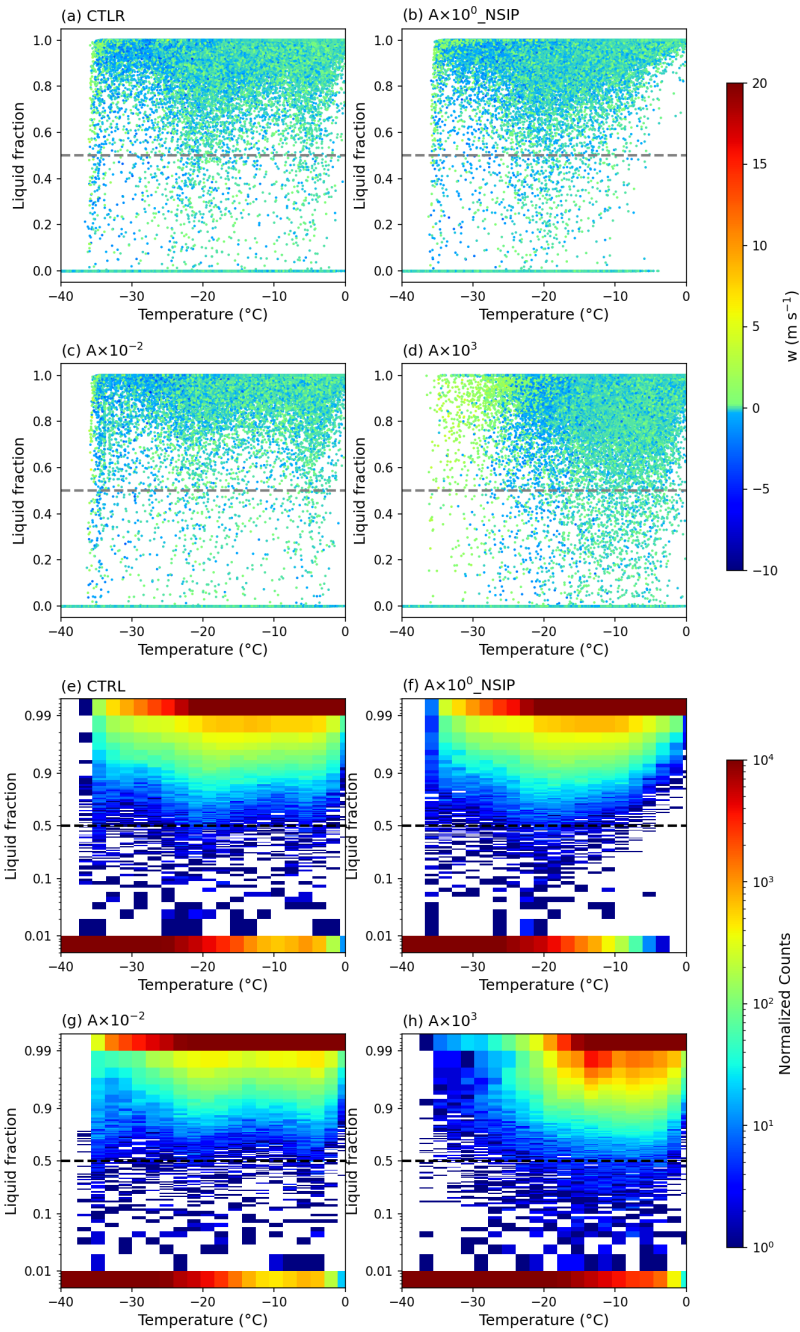
1182

1183

Figure 5: Spatial- and time-averaged (9:00~19:00) profiles of process rates of (a) heterogeneous freezing (immersion and deposition nucleation), (b) homogeneous freezing, (c) secondary-ice production (rime-splintering), (d) cloud droplets rimed with ice crystals, (e) rain droplets rimed with ice crystals, (f) collection between ice and ice. Unit is $\text{g kg}^{-1} \text{s}^{-1}$. The average mixed-phase layer ($0 \sim -38^\circ\text{C}$) is roughly in between 3.2 and 8.6 km. Shaded area indicates the spatial- and time-averaged mixed-phase region. Unit is $\text{g kg}^{-1} \text{s}^{-1}$.

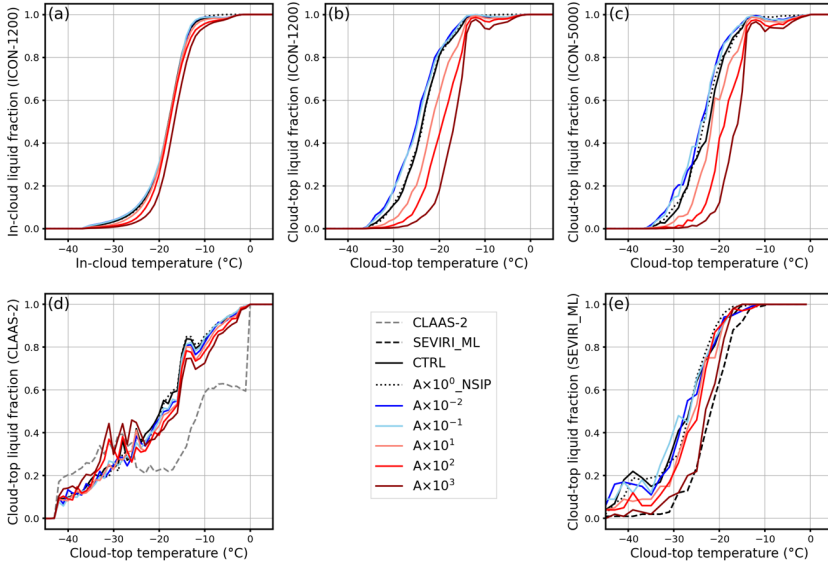


1187 Figure 6: In-cloud supercooled liquid mass fraction distribution as a function of
1188 temperature (binned by 1°C) between 9:00 and 19:00 (a-d) for the 4 cases ($A \times 10^0$,
1189 $A \times 10^0_{\text{NSIP}}$, $A \times 10^{-2}$, $A \times 10^3$), the colour of points indicates the vertical wind velocity
1190 (unit, m s^{-1}). 2-D histogram of in-cloud liquid mass fraction versus temperature (e-f).



1193 Figure 7: Cloud-top supercooled liquid mass fraction distribution as a function of
1194 temperature (binned by 1°C) between 9:00 and 19:00 (a-d) for the 4 cases ($A \times 10^0$,
1195 $A \times 10^0_{\text{NSIP}}$, $A \times 10^{-2}$, $A \times 10^3$), the colour of points indicates the vertical wind velocity
1196 (unit, m s^{-1}). 2-D histogram of cloud-top liquid mass fraction versus temperature (e-f).

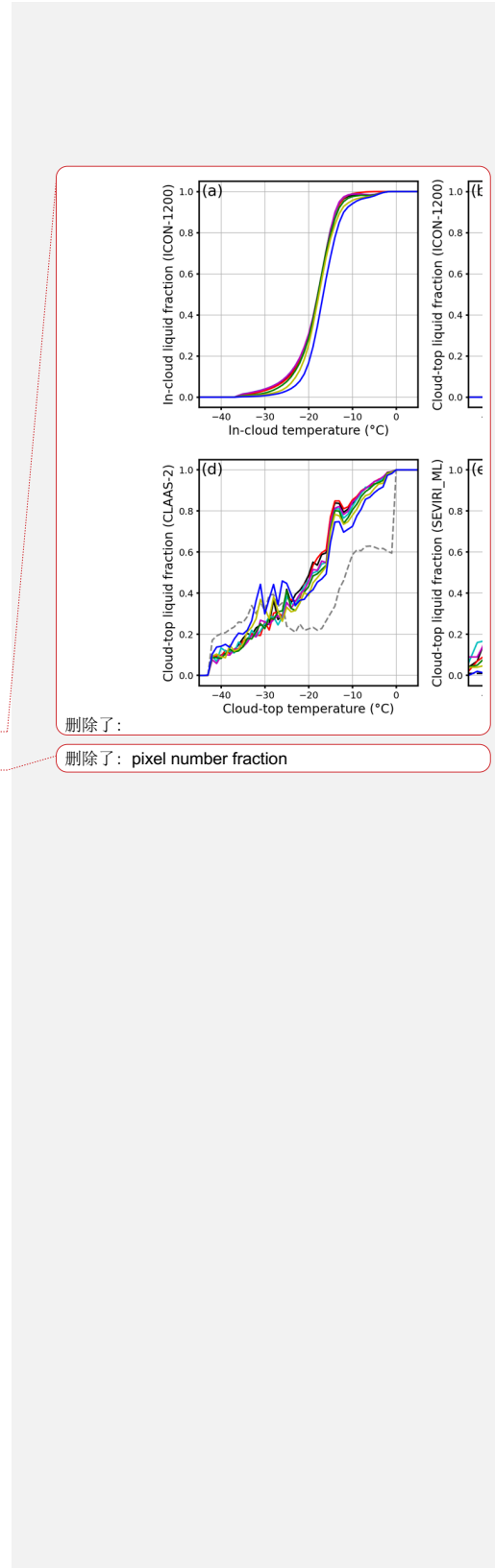
1197



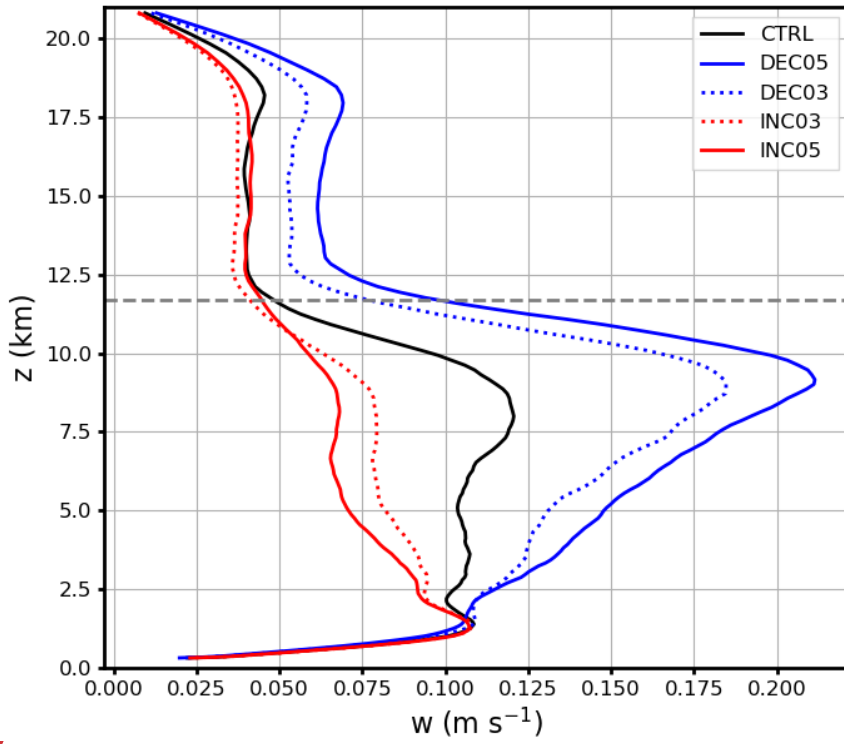
1198

1199 Figure 8: Liquid cloud pixel fraction as a function of temperature from 9:00 to 19:00
 1200 UTC for the INP sensitivity experiments, (a) in-cloud fraction calculated from
 1201 simulations on ICON native grid (~1200 m), (b) cloud-top fraction calculated from
 1202 simulations on ICON native grid (~1200 m), (c) cloud-top fraction calculated from
 1203 simulations on SEVIRI's grid (~5000 m), (d) cloud-top fraction calculated by remote-
 1204 sensing retrieval algorithms to produce CLAAS-2 dataset, and (e) cloud-top fraction
 1205 calculated by remote-sensing retrieval software suite SEVIRI_ML. The temperature
 1206 is binned by 1°C in (a), (b), (c), and (d), and by 2°C in (e).

1207



1210



1211

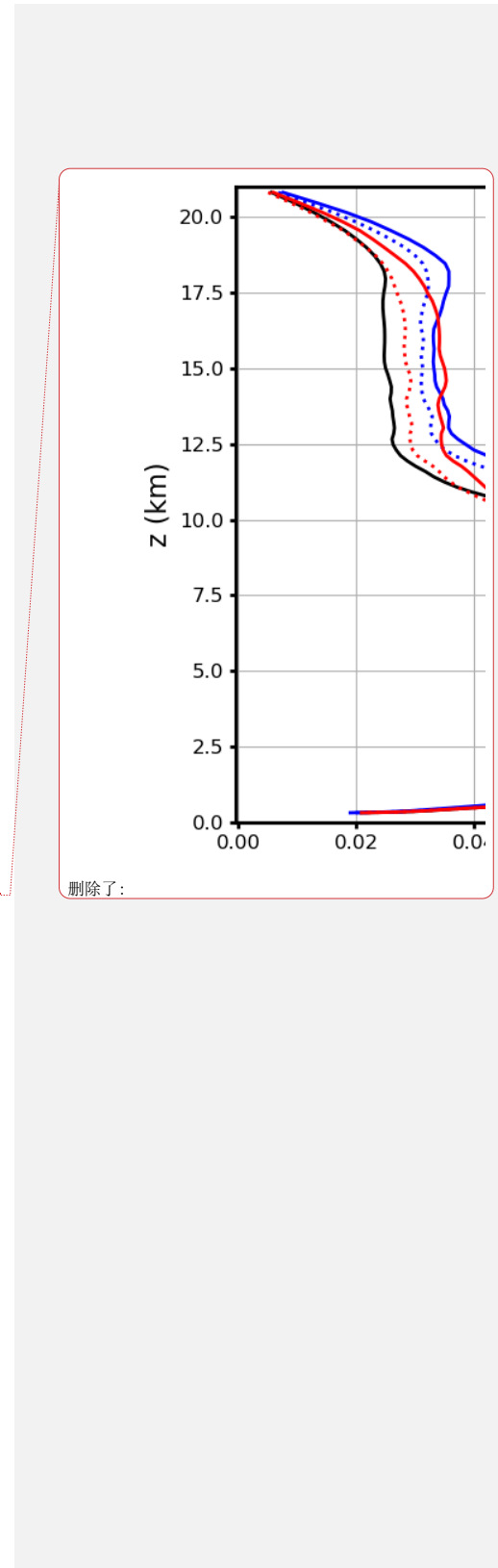
1212

1213

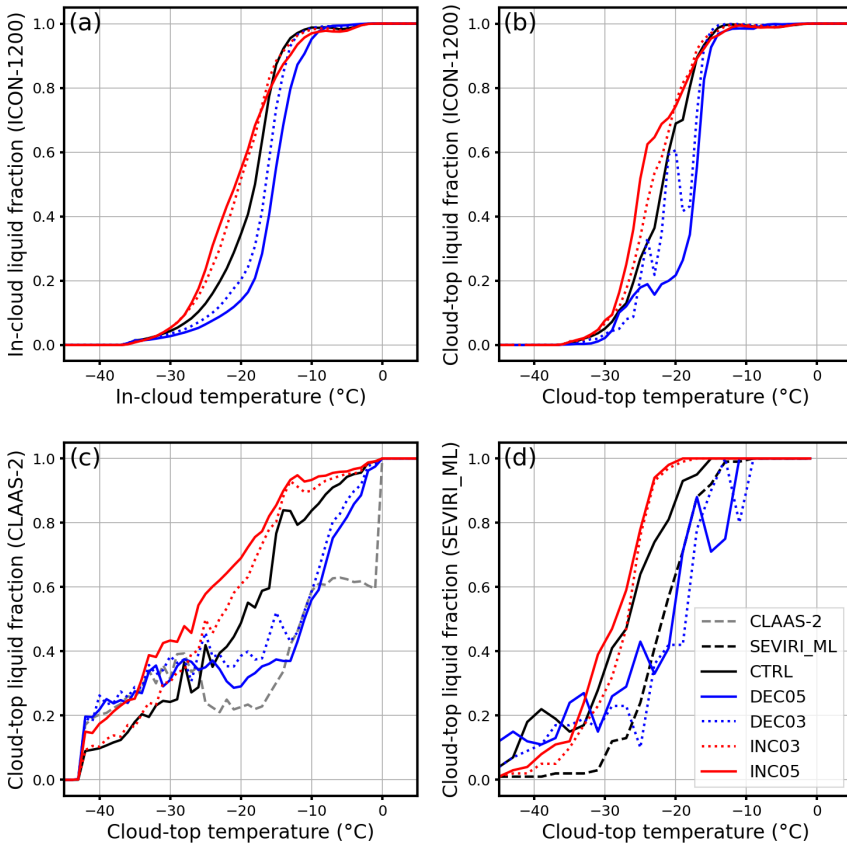
1214

1215

Figure 9: Spatial- and time-averaged (9:00~19:00) profiles of vertical velocities (w values $\leq 0 \text{ m s}^{-1}$ are excluded). The dashed grey line indicates the clout top height which is about 11.7 km.



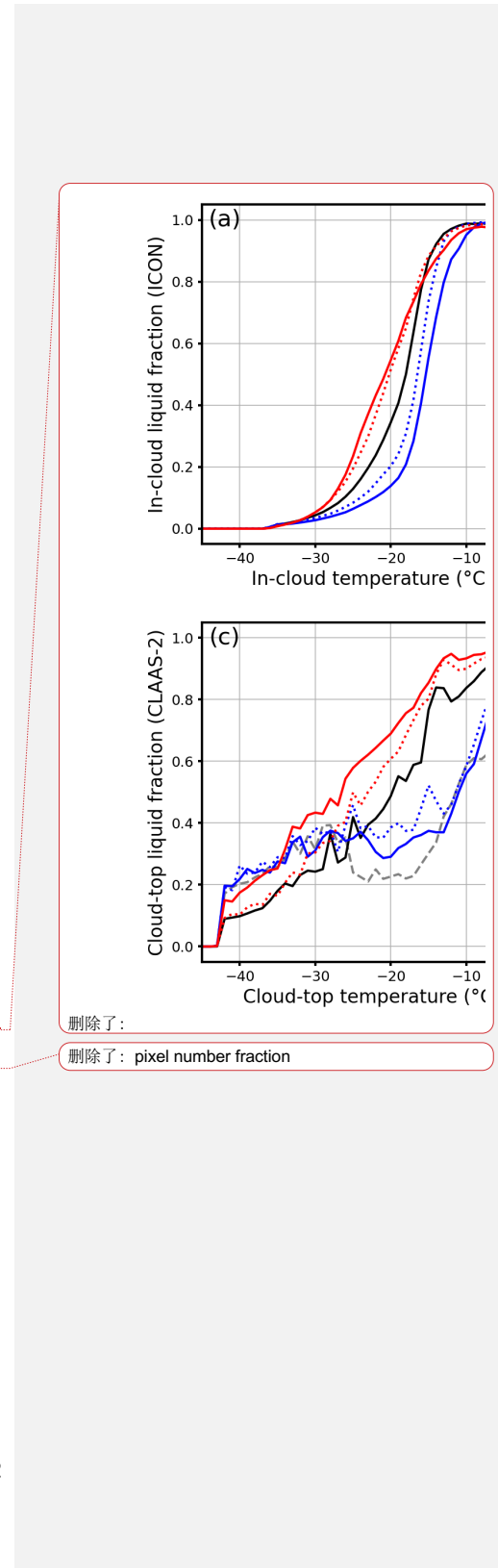
1217



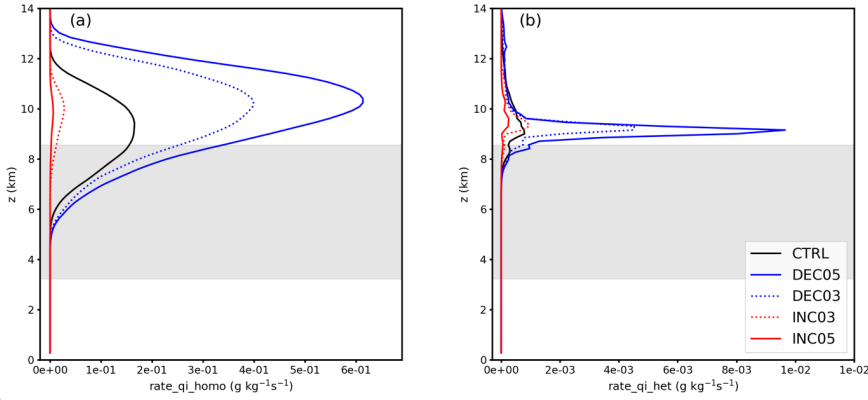
1218

1219 Figure 10: Liquid cloud pixel fraction as a function of temperature from 9:00 to 19:00
 1220 for the thermodynamic sensitivity experiments, (a) in-cloud fraction calculated
 1221 directly from simulations, (b) cloud-top fraction calculated from directly simulations,
 1222 (c) cloud-top fraction calculated by remote-sensing retrieval algorithms to produce
 1223 CLAAS-2 dataset, and (d) cloud-top fraction calculated by remote-sensing retrieval
 1224 software suite SEVIRI_ML. The temperature is binned by 1°C in (a), (b), and (c), and
 1225 by 2°C in (d).

1226



1229



1230

1231 Figure 11: Spatial- and time-averaged (9:00~19:00) profiles of process rates of (a)
1232 homogeneous freezing, (b) heterogeneous freezing (immersion and deposition
1233 nucleation) for cases with perturbed initial thermodynamic states. Shaded area
1234 indicates the spatial and time-averaged mixed-phase region. Unit is $\text{g kg}^{-1} \text{s}^{-1}$.

1235

